J. Fluid Mech. (1990), *vol.* 215, *pp.* 229–262
Printed in Great Britain

Direct numerical simulation of two-dimensional turbulent natural convection in an enclosed cavity

By SAMUEL PAOLUCCI†

Applied Mechanics Department, Sandia National Laboratories, Livermore, CA 94550, USA

(Received 21 January 1988 and in revised form 18 October 1989)

A two-dimensional direct numerical simulation of the natural convection flow of air in a differentially heated square cavity was performed for a Rayleigh number of 10^{10}. The simulation was commenced from isothermal and quiescent conditions and was allowed to proceed to a statistical steady state. Two-dimensional turbulence resulted without the introduction of random forcing. Good agreement of mean quantities of the statistically steady flow is obtained with available experimental results. In addition, the previously proposed (George & Capp 1979) $-\frac{1}{3}$ and $+\frac{1}{3}$ temperature and velocity variations in the buoyant sublayer are confirmed. Other statistics of the flow are consistent with available experimental data. Selected frames from a movie generated from the computational results show very clearly turbulence production via the sequence from initial instability, proceeding through transition, and eventually reaching statistical steady state. Prominent large-scale structures are seen to persist at steady state.

1. Introduction

One of the fundamental flow configurations for heat transfer and fluid mechanics studies is the turbulent natural convection flow within a differentially heated vertical cavity. This configuration is relevant to many engineering applications, and is of considerable practical interest. Applications include reactor insulation, cooling of radioactive waste containers, ventilation of rooms, solar energy collection, and others. While there has been substantial work devoted to the study of turbulent natural convection in the Rayleigh–Bénard problem where the gravitational vector is parallel to an imposed thermal gradient (e.g. Lipps 1976; Grötzbach 1982), relatively minor attention has been given to the case where gravity is orthogonal to the gradient. There are only a few publications on this subject and the published experimental data are insufficient to fully characterize the mechanisms responsible for momentum and heat transport in the thermal layers. In contrast, theoretical and experimental studies for the same problem but in the laminar regime are abundant. For example, see Elder (1965*a*), Cormack, Leal & Imberger (1974), de Vahl Davis & Jones (1983), and Chenoweth & Paolucci (1986) (referred to as CP henceforth), and references therein.

In a vertical layer that is bounded by vertical isothermal surfaces having different temperatures and thermally insulated at the ends, a circulatory flow is set up, ascending against the hot surface and descending at the cold surface. It is well known (from both experimental and numerical simulations in the laminar boundary layer regime, and experimental in the turbulent regime) that, at steady state, the

---

† Present address: Department of Aerospace and Mechanical Engineering, University of Notre Dame, Notre Dame, IN 46556, USA.

temperature away from the boundary layers increases linearly over a large part of the height of the layer (Eckert & Carlson 1961; Elder 1965*b*; Kutateladze, Kirdyashkin & Ivakin 1972*b*; CP). Consequently, the vertical cavity is also important from the point of view of investigating the structure of a turbulent free-convection boundary layer in the presence of stable stratification. As will be shown, the structure of the boundary layer is related to that of an isolated heated or cooled vertical flat plate.

The flow in the cavity passes through several stages as the fluid flows along the active vertical walls. The flow near the entry corners of the boundary layers is initially laminar. It then passes through a transition region, and finally becomes turbulent. When a statistical steady state obtains, the space between the vertical boundary layers is filled by a virtually immobile stably stratified fluid executing low-frequency, low-velocity oscillations.

One of the earliest experimental studies of this problem was performed by Mull & Reiher and has been discussed by Jakob (1949) and Batchelor (1954). Subsequently Mordchelles-Regnier & Kaplan (1963) have obtained some measurements and visualizations up to Rayleigh numbers of order 10^{12}. These early works were followed by the classic experimental work of Elder (1965*b*), who measured primarily the temperature and velocity in the cavity using several fluids of high Prandtl number. He concluded that the occurrence of the turbulent wall layers in the cavity is independent of the aspect ratio and occurs in a similar manner to that on an isolated vertical plate. More recently MacGregor & Emery (1969) experimentally obtained heat transfer data for different Prandtl numbers and aspect ratios; Kutateladze *et al.* (1972*b*, 1977, 1978) measured heat transfer, velocity and temperature means, their fluctuations, as well as the probability density distribution of temperature fluctuations; Cowan, Lovegrove & Quarini (1982) obtained overall and local heat transfer data for different aspect ratios; Kirdyashkin *et al.* (1983), and Kirdyashkin & Semenov (1984) measured the temperature means, fluctuations and their frequency spectra, the temperature kurtosis and skewness parameters, as well as other turbulence quantities; and Giel & Schmidt (1986) obtained velocity and temperature means and fluctuations, as well as frequency spectra of temperature fluctuations.

In the present work we consider the nonlinear physics of turbulence numerically. More specifically, we perform a *direct* numerical simulation of the free convective flow in a vertical cavity across which a uniform temperature difference is maintained. Although the initial conditions used herein are non-random, owing to strong buoyancy the flow breaks up into an apparently *random* one. In this work a flow which exhibits temporal as well as spatial randomness is identified as being turbulent.

The flow is assumed to be two-dimensional. Although physical flows are usually three-dimensional, two-dimensional turbulence is often considered as a first approximation in many cases (e.g. turbulent flows submitted to a stable stratification). Furthermore, it appears from numerous experiments dealing with this problem (e.g. Giel & Schmidt 1986), and the related problem of natural convection from a heated vertical plate (e.g. Lochet, Lemonnier & Doan-Kim-Son 1983), that three-dimensionality in this class of flows has a very small influence if the depth dimension is not too small. In this connection, it is noted that the inertial subrange of two-dimensional turbulence is quite different from that in three-dimensions (Kraichnan 1967; Lilly 1969). In particular, in inviscid isothermal flow the cascade of energy in two dimensions is mainly toward low wavenumber in the inertial range, and becomes weak or non-existent at higher wavenumbers where only vorticity variance or enstrophy is cascaded in the usual sense in the inertial range.

Turbulence consists of chaotic motion in space as well as in time, and often persistent organized motions as well, at range of scales that increase rapidly with Reynolds number. Over two decades ago Corrsin (1961) demonstrated that the direct numerical simulation of high-Reynolds-number flows places an overwhelming demand on computer memory and speed. The convective terms of the equations produce a range of scales limited by molecular diffusion, so that with sufficiently low Reynolds number the entire range can be numerically resolved and no modification of the governing equations is required. When computer capacity does not allow complete resolution and the equations are not modified to take this into account, the computed values for higher Reynolds numbers may have no relation to fluid physics. The basic problem is accuracy in calculating the small scale of some of the turbulent eddies. As the turbulence strength and/or time increases, smaller eddies are generated. No matter how small the numerical mesh size, one can always choose a Reynolds number and/or time large enough that the results will be quantitatively inaccurate. One way of improving the accuracy is to resolve all the eddies containing almost all the energy. By assuming that the flow is two-dimensional this demand is alleviated somewhat. The numerical simulation is still difficult since the flow is totally bounded by solid walls and at the same time is buoyantly driven. The complication due to the solid walls is handled by the use of an adaptive non-uniform grid scheme which allows sufficient resolution next to the walls. The complication due to buoyancy is not just cosmetic, since the actual equations solved do not embody the usual Oberbeck–Boussinesq approximation, and hence are capable of treating more general problems, even though in the present work density variations are restricted to be very small so as to be well within the Oberbeck–Boussinesq limit.

The study of the time-dependent structure of turbulence and determination of the average characteristics of the flow and heat transfer using numerical modelling, omitting the usual averaging, involves not only solution of difficult numerical problems, but also creation of special processing systems and methods of analysis. The use of a graphics post-processor which allows the examination of the flow structure during the transition from laminar to turbulent flow, as well as the fine structure of the wall layers, was found to be indispensable in this work. The use of stored simulation results allowed rapid interactive display of results, and at the same time placed fewer constraints on the questions that could be answered regarding the flow.

The purpose of this paper is two-fold. First, to present results which should be helpful in constructing simplified turbulence models for natural convection flows. Secondly, to show that the prevailing theories of heat and mass transfer which assume relationships for friction and heat transfer similar to those in forced boundary-layer flow, are not applicable to natural convection turbulence. This paper is presented in four sections. Section 2 presents the governing equations and details the formulation of the numerical problem. Results of the simulation and comparisons with relevant experimental data are presented in §3. Finally we conclude in §4 with a summary of the major results.

2. Formulation of the numerical problem

2.1. *Equations, and boundary and initial conditions*

Consider a two-dimensional rectangular cavity of width L and height H filled with air. The air is initially quiescent at a uniform temperature T_0 and pressure p_0. The walls of the vessel are initially at the same temperature T_0. At times larger than zero, the left and right walls are maintained at temperatures of T_h and T_c, respectively, where $T_\mathrm{h} > T_\mathrm{c}$. The top and bottom walls are insulated. We non-dimensionalize the problem by reference quantities for length, velocity, and temperature using the cavity width L, the thermal diffusion speed α/L, and the mean of the wall temperatures $T_\mathrm{r} = \frac{1}{2}(T_\mathrm{h} + T_\mathrm{c})$, respectively.

The problem evolves in time t and can be described in two-dimensions in terms of the velocity components $v_i = (u, v)$ in the $x_i = (x, y)$ directions, the density ρ, temperature T, and pressure p. The governing equations are statements of conservation of mass, momentum, and energy, with the addition of the ideal gas law. These equations, valid under a small-Mach-number approximation, but allowing for arbitrary density variations, have been derived by Paolucci (1982), and have been used to investigate the solutions of related problems in the laminar regime in CP, and in the transition regime in Paolucci & Chenoweth (1989) (hereafter referred to as PC). They are given as follows:

$$\frac{\partial \rho}{\partial t}+\frac{\partial \rho v_j}{\partial x_j}=0, \tag{2.1}$$

$$\frac{\partial \rho v_i}{\partial t}+\frac{\partial}{\partial x_j}(\rho v_j v_i)=-\frac{\partial \Pi}{\partial x_i}+\frac{Ra\,Pr}{2\epsilon}\rho n_i+Pr\frac{\partial}{\partial x_j}\tau_{ij}, \tag{2.2}$$

$$\rho c_p\left(\frac{\partial T}{\partial t}+v_j\frac{\partial T}{\partial x_j}\right)-\Gamma\frac{\mathrm{d}\bar{p}}{\mathrm{d}t}=\frac{\partial}{\partial x_j}\left(k\frac{\partial T}{\partial x_j}\right), \tag{2.3}$$

$$\bar{p}=\rho T, \tag{2.4}$$

where $\Pi = p^{(1)}/(\gamma Ma^2)$ is a reduced pressure which accounts for the hydrostatic and dynamic effects, $p^{(1)}$ is the second term in the Mach-number expansion of p and is $O(Ma^2)$, γ is the ratio of specific heats, n_i is the unit vector in the direction of gravity, τ_{ij} is the viscous stress tensor given by

$$\tau_{ij}=\mu\left(\frac{\partial v_i}{\partial x_j}+\frac{\partial v_j}{\partial x_i}\right)-\tfrac{2}{3}\delta_{ij}\mu\frac{\partial v_k}{\partial x_k},$$

δ_{ij} is the Kronecker delta function, and $\Gamma = (\gamma-1)/\gamma$ is a measure of the resilience of the fluid. The thermal conductivity, viscosity, and specific heat at constant pressure are functions of the thermodynamic variables. Note that the Mach number only serves as a scaling for the dynamic and hydrostatic components of pressure.

The spatially uniform pressure $\bar{p} = p^{(0)}(t)$ appearing in the energy equation and the equation of state, which represents the first term in the expansion of p, accounts for the change of the static pressure with time. The separation of the pressure components, holding under the small-Mach-number approximation, is the essence of the acoustic wave 'filtering'; however, this splitting introduces $\bar{p}$ as an extra unknown. It can be shown that the equation for $\bar{p}$ is obtained by a global mass conservation statement and the use of boundary conditions.

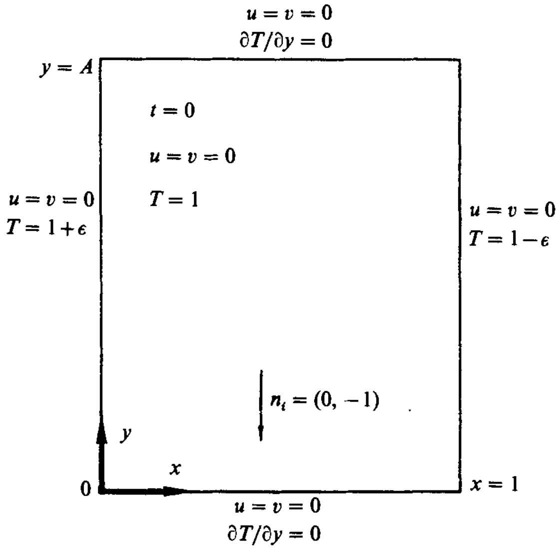

FIGURE 1. Problem definition.

The initial and boundary conditions used, expressed in dimensionless form, are

$$v_i(x_j, 0) = 0, \quad T(x_j, 0) = 1, \tag{2.5}$$

$$\left.\begin{aligned} v_i(0,y,t) = v_i(1,y,t) = v_i(x,0,t) = v_i(x,A,t) = 0,\\ T(0,y,t) = 1+\epsilon, \quad T(1,y,t) = 1-\epsilon,\\ \frac{\partial T}{\partial y}(x,0,t) = \frac{\partial T}{\partial y}(x,A,t) = 0. \end{aligned}\right\} \tag{2.6}$$

It is noted that in the Boussinesq limit $\epsilon \rightarrow 0, \bar{p} \rightarrow 1$, and the relevant independent dimensionless parameters appearing in the problem are the Rayleigh number, the Prandtl number, and the aspect ratio:

$$Ra = \frac{\beta \Delta T g L^3}{\nu\alpha}, \quad Pr = \frac{\nu}{\alpha}, \quad A = \frac{H}{L}. \tag{2.7}$$

In the above definitions ν and α are the kinematic viscosity and thermal diffusivity respectively, β is the coefficient of thermal expansion, g is the magnitude of the gravitational field, and $\Delta T = T_h - T_c$.

The problem is illustrated in figure 1. In this paper we use $\epsilon = \Delta T/2T_0 = 1/566$, $A = 1$, $Pr = 0.71$, and $Ra = 10^{10}$. Because of the centro-symmetry property of the Oberbeck–Boussinesq equations for this problem, had those equations been used to obtain the solution, a laminar flow would have resulted even at this high Rayleigh number (representing an unstable branch in a stability diagram). To break the symmetry, the introduction of a non-physical perturbation with an arbitrary wavelength would have been necessary, hence effecting the transient path to the ultimate turbulent regime. In contrast, the set of equations used do not possess this symmetry property, and hence mathematically unstable branches cannot be obtained. Furthermore it is believed that the path to turbulence should more closely follow that of the real physical problem since property variations are treated accurately and consistently.

2.2. *Finite-difference equations*

Numerical implementation of the governing equations consists of four main issues: numerical approximation of spatial derivatives, a time advancement algorithm, initial and boundary conditions, and computer implementation and organization. In each category there are options available, and the choice of the overall algorithm depends on the problem under consideration, the cost, and the computer architecture. I will touch on each of these subjects.

There are several ways to formally deduce a finite-difference scheme from the basic equations. For a review of the methods which have become important for direct numerical simulation, the reader is referred to the papers of Love (1979) and Schumann, Grötzbach & Kleiser (1980). The numerical scheme employed is based on explicit finite differences using a staggered mesh. To derive the finite-difference equations one starts by overlaying a staggered grid network over the region of interest. The grids are allowed to be non-uniform and mutually orthogonal in Cartesian coordinates. The differential equations are averaged on a local two-dimensional grid volume to obtain their finite-difference form. This procedure, without the additional complexity of non-uniform grids, is described by Grötzbach (1982), where the reader is referred for more details.

To accurately describe boundary heat fluxes in unsteady boundary layers with a minimum of node points, especially at very small times, it is necessary to use a non-uniform coordinate mesh with dynamic rezoning. The need for non-uniform grids arises since the smallest grids necessary near the boundaries can sometimes be orders of magnitude smaller than needed well outside the boundary layers. The approach used is described in detail in PC. Briefly, the non-uniform grid is transformed to a uniform one by an orthogonal tranformation $\xi_k = \xi_k(x_k)$ which also maps the problem to the computational domain $-1 \leqslant \xi_k \leqslant 1$, where $x_k = (x, y)$ and $\xi_k = (\xi, \eta)$. After specification of a function describing the grid variation in the x_i-plane, all that is left to completely specify the non-uniform grid are the parameters S_i which are used to control the grid reduction in the boundary layers as functions of time. The parameters S_i measure the ratios of the smallest to largest grids. The way they are controlled is based on boundary flux error. For example, S_y is discretized as $S_y(t_n) = S_y^n$, and an initial grid reduction value is specified, e.g. $S_y^0 = 10^{-2}$ (note that $S_y \equiv 1$ gives a uniform grid). At the location of maximum wall heat flux, the numerical value of $(\partial T/\partial y)^n$ is evaluated using both linear and quadratic interpolations L_y^n and Q_y^n, respectively. If we let $\epsilon_y^n = |1-L_y^n/Q_y^n|$, and ϵ_y^m be an error control parameter, then the grids can be controlled as follows: let

$$S_y^{n+1} = S_y^n[1+H_y^2(\epsilon_y^m-\epsilon_y^n)],$$

where $H_y = L_y \tanh^{-1} L_y$, and $L_y = (1-S_y^n)^{\frac{1}{2}}$, then

$$S_y^0 \leqslant S_y^{n+1} \leqslant 1. \tag{2.8}$$

It was found by Chenoweth & Paolucci (1981) that if ϵ_y^m is chosen within the range $0.03 \leqslant \epsilon_y^m \leqslant 0.10$, then one can be assured that several grid points remain in the boundary layer, but no more than necessary to obtain the accuracy desired. For the present problem, since we have two coordinate directions, the above transformation is used in each coordinate with $S_x^0 \neq S_y^0$ in general.

Time advancement may be done either explicitly or implicitly. The first-order explicit Euler scheme was chosen since it was easy to implement, has a much lower cost per time step, and requires much less computer memory allocation than an equivalent implicit implementation. The stability of the scheme was found to be governed by the local grid Péclet number near the vertical walls.

The finite-difference equations are solved on the adaptive staggered grid system using an explicit predictor–corrector scheme with forward differences for time derivatives and central differences for spatial derivatives, with a truncation error $O(\Delta t, \Delta \xi_i^2)$. The computational procedure is described by CP who solved the related problem in the laminar regime. The reader is referred to that work for the details. The only modification to that procedure is the computation of a new grid before the time is incremented.

Finite-difference approximations of the nonlinear terms contain aliasing errors. These errors are usually less severe than corresponding ones obtained using spectral methods owing to the damping at high wavenumbers of the difference approximation. These errors usually increase with the order of accuracy of difference schemes. Lilly (1965) demonstrated that the staggered-mesh difference scheme used above preserves invariance properties of the original equations such as conservation of mass, momentum, energy, and circulation. Aliasing errors can violate these invariance properties and lead to nonlinear numerical instabilities. Thus it is felt that using a staggered mesh with second-order spatial accuracy, a time integration using a first-order explicit Euler scheme, accompanied by grids and time steps small enough to resolve the small scales would give us a sufficiently accurate solution.

2.3. *Resolution requirements*

In natural convection problems, it is well known that turbulence can be sustained at relatively low Reynolds numbers. Furthermore, as already mentioned, the two-dimensional assumption appears to be justified for the problem being considered. Both of these facts, combined with a judicious grid distribution, make a direct simulation possible. It remains now to choose appropriate grid sizes to resolve the complete flow. Since any effects due to eddies smaller than the grid size are neglected, as pointed out by Grötzbach (1983) we must have a grid distribution that allows the resolution of steep gradients in the velocity and temperature fields near the walls, and mean grid widths smaller than the smallest relevant turbulence elements. Quantifying these qualitative criteria can be a difficult problem.

For high Rayleigh numbers, the thickness of the boundary layer is small compared with the dimensions of the cavity. Thus, it is expected that in the vicinity of an active wall, the boundary layer should be similar to that arising from an isolated vertical plate. Since no wall model is provided in the computer simulation, then it is necessary to resolve the conductive sublayer. It is reasonable to assume that the thickness of the thermoviscous sublayer should be of the same order or larger than the conductive sublayer since the flow is driven by thermal effects.

Using a scaling analysis and experimental results of Smith (1972), George & Capp (1979) show that the conductive sublayer on a warm isolated vertical plate immersed in an isothermal environment extends to

$$x \approx 1.7(Pr\, Ra_{\mathrm{m}})^{-\frac{1}{3}}. \tag{2.9}$$

The subscript 'm' denotes that the Rayleigh number is based on $\Delta T_{\mathrm{m}} = T_{\mathrm{w}} - T_{\mathrm{m}}$, where T_{w} is the temperature of the plate, and T_{m} is the temperature outside the boundary layer ($T_{\mathrm{m}} = T_{\infty}$ for an isolated plate). The above result was also recently confirmed by Siebers, Moffatt & Schwind (1985) but with a constant of approximately 3. In the case of the cavity $\Delta T_{\mathrm{m}} = \frac{1}{2}\Delta T$ at early time, and it is approximately a linear function of the vertical coordinate when the flow becomes stationary (e.g.

Kutateladze *et al.* 1977; Cowan *et al.* 1982). In the Oberbeck–Boussinesq limit this linear function has a non-dimensional slope of approximately 0.36.

As noted by Grötzbach (1983), in order to resolve very small eddies close to the dissipation scale, for $Pr < 1$ we must have $\Delta \leqslant \pi(\nu^3/\varepsilon)^{\frac{1}{4}}/L$, where $\Delta = (\Delta x\,\Delta y)^{\frac{1}{2}}$ is the mean grid size, and ε is the rate of energy dissipation per unit mass. Since most of the energy is dissipated on scales larger than Δ, resolution of these scales would seem to be sufficient. If it is assumed that ε is constant and equal to the production of energy, then $\varepsilon = \bar{k}^{\frac{3}{2}}/L$, where $\bar{k}$ is the mean turbulent kinetic energy. Now $\bar{k}$ can be estimated by making use of equations for the mean turbulence kinetic energy and mean-squared temperature fluctuations (see (3.28) and (3.29)) and assuming local equilibrium where production is balanced by dissipation. Alternatively, an upper bound for $\bar{k}$ can be obtained by using some fraction of the free buoyancy speed $(\beta g\,\Delta TL)^{\frac{1}{2}}$. For large-Rayleigh-number laminar flow in the boundary-layer regime, the maximum speed is approximately $\frac{1}{4}$ of the free buoyancy speed at steady state (see CP). From the above considerations based on Kolmogorov scaling, in order to resolve the microscopic lengthscale, we must have approximately

$$\Delta \leqslant \pi(16Pr/Ra)^{\frac{3}{8}}. \qquad (2.10)$$

In the centre of the cavity the mean speed is approximately zero, so that larger grid sizes can be used. In addition, the above estimate is expected to be somewhat smaller than necessary since it is based on an estimate of the maximum speed in laminar flow.

Using similar arguments, an estimate of the dimensionless Kolmogorov timescale $\pi\alpha(\nu/\varepsilon)^{\frac{1}{2}}/L^2$ required to resolve the microscopic motion can be provided. The result is that we must have approximately

$$\Delta t \leqslant 8\pi\,Pr^{-\frac{1}{4}}Ra^{-\frac{3}{4}}. \qquad (2.11)$$

In order to quantify the resolution requirements for our particular problem, values of parameters specified in the actual computation must be used. For $Pr = 0.71$ and $Ra = 10^{10}$, (2.9)–(2.11) require $\Delta x \leqslant 1.11 \times 10^{-3}$ near the active walls in order to resolve the conductive sublayer, a mean grid size of the order $\Delta \leqslant 1.39 \times 10^{-3}$ and an integration time step of the order $\Delta t \leqslant 8.66 \times 10^{-7}$ to resolve the microscopic length- and timescales, respectively, in the boundary layers.

The computational domain was discretized using 121×121 control volumes. The following values of grid-control parameters were used at the initial time: $\epsilon_x^m = \epsilon_y^m = 0.03$, $S_x^0 = S_y^0 = 0.01$. Throughout the computation, ϵ_x^m and ϵ_y^m are held fixed, while S_x^n and S_y^n vary according to the demands of the solution. When statistical steady state was achieved S_x^n and S_y^n had the values of 0.0158 and 0.0203, respectively, and the corresponding grid distribution is shown in figure 2. At the initial time $\Delta x_{\max}/\Delta x_{\min} = \Delta y_{\max}/\Delta y_{\min} \approx 195$, and $1.27 \times 10^{-4} \leqslant \Delta \leqslant 2.48 \times 10^{-2}$, Δ being smallest in the corners of the cavity, and largest in the centre. In regions of high gradients near the active walls at $y = \frac{1}{2}A$, we have $\Delta \approx 1.78 \times 10^{-3}$ and $\Delta x \approx 1.27 \times 10^{-4}$. The respective values at steady state are $\Delta x_{\max}/\Delta x_{\min} \approx 124$, $\Delta y_{\max}/\Delta y_{\min} \approx 96$, $2.06 \times 10^{-4} \leqslant \Delta \leqslant 2.25 \times 10^{-2}$, and $\Delta \approx 2.02 \times 10^{-3}$ and $\Delta x \approx 1.86 \times 10^{-4}$ near the walls at $y = \frac{1}{2}A$. Note that although the mean grid width does not change much throughout the entire calculation, the values of Δx and Δy change substantially as shown by the change in grid ratios. The time step changed somewhat during the computation depending on the demands of the solution. The average value was found to be $\Delta t_{\text{ave}} = 2.73 \times 10^{-9}$.

As is readily apparent (and not coincidentally) the conductive sublayer was well resolved. In fact, we have 6 grid points within each sublayer at $y = \frac{1}{2}A$ when the flow

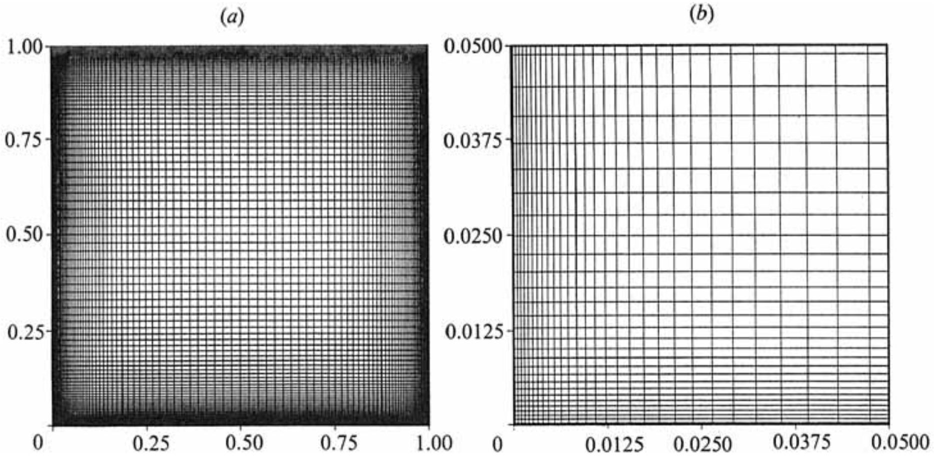

FIGURE 2. Grid distribution at statistical steady state: (*a*) complete cavity, (*b*) detail of lower left corner showing 1/400th of the total area.

is stationary. Moreover, the adaptive grid algorithm demanded approximately 10 points inside the vertical velocity maximum and a total of approximately 30 points within each boundary layer at stationarity. Since the resulting mean grid width within the boundary layer and near the corners of the cavity, and the integration time step are of the same order or smaller than the estimated Kolmogorov scale requirements, it is felt that the flow should be resolved down to the microscales. Note that the mean grid width in the core of the cavity is approximately one order of magnitude larger than the microscopic lengthscale. It is felt that this fact should not impair the resolution since in the core of the cavity energy production should be very much smaller than in the boundary layers or corner regions.

More than 3.5×10^5 time steps were computed. The simulation encompassed a total time $t = 9.55 \times 10^{-4}$ (measured on a diffusion timescale). Detailed statistics were obtained from more than 10^4 samples of velocity and temperature profiles on the mid-sections of the cavity obtained during the time interval $6.81 \times 10^{-4} \leqslant t \leqslant 9.55 \times 10^{-4}$. The sampling period was $\Delta t = 2.5 \times 10^{-8}$.

The calculations were performed over a period of several months on a CRAY-1S computer. The computer time required to obtain a statistical steady state was approximately 85 hours. The calculations were carried out for an additional 70 hours to obtain a sufficient number of samples for meaningful statistics at the lower frequencies. The determination of the time at which stationarity was achieved was obtained from inspection of the temperature and velocity fields at different times, hence it is very subjective. However, statistics obtained using one-half and one-quarter of the sample size differed very little from that obtained from the full sample hence verifying the assumption of stationarity. Subsequently, all statistical data reported were obtained from the full sample of over 10^4 data points.

2.4. *Graphics post-processing*

A computational fluid dynamics solution of the Navier–Stokes equations results in values of the dependent variables at discrete points in the field within the geometry of interest. Not including the special data required for statistics, and because of the unsteady nature of the problem, 156 million words of data were generated when approximately 2000 time steps were saved. Use of interactive graphics provided the only practical means of analysing such an enormous data set, and a graphics post-processor, developed specifically for this computer program, proved invaluable in visualizing and understanding the resulting solutions of the calculations. The advantage of interactivity is that one can discover information that might not be anticipated.

Interactive graphics are used to interpret the computed flow solution by looking at different regions within the cavity and plotting different flow quantities. Quantities describing the flow field are characterized by magnitude and direction, and a variety of displays are used to extract this information. Scalar quantities such as temperature are displayed by sectional profiles, isoline levels, and colour shading using scan-line rendering. Vector quantities such as velocity are illustrated by displaying arrows, where both magnitude and direction are represented. With the use of velocity vectors the existence of flow separation can be easily seen. It is noted that in displaying the velocity fields only vectors on an interpolated matrix of 25×25 evenly spaced grids are shown for clarity of presentation, even though the number of computed values is obviously much greater. Because of this, the ability to zoom in on a field display was found to be extremely important.

By generating a movie, the additional dimension of time can be displayed. For unsteady flow computations the demonstration of the physics involved can only be done using motion. The flow is in motion, and to present it through a movie is only natural. As a result, many of the time-dependent phenomena, such as turbulence generation, cannot be fully appreciated in the still pictures presented in this paper.

3. Results

In this section we shall often compare our results with those of experiments. All relevant experiments (i.e. in the turbulent regime) known to the author either involve vertical plates with $Pr \approx 0.7$ but no vertical stratification, or cavities with $Pr \geqslant 7$ and generally large aspect ratios, but having stratified cores. The computational results can only be compared with the first class of experiments near the wall where Prandtl-number effects are important and stratification is not, and with the second class only in the exterior regions of the boundary layer and core where Prandtl-number effects are small (because of turbulence), and aspect-ratio differences can be accounted for in comparing the important stratification effects.

3.1. *The approach to stationary flow*

Figure 3(*a–l*) (Plates 1, 2 and 3) displays details of the transient temperature and velocity fields from early times to stationarity. The colours red and blue respectively denote warm and cold temperature with values in between corresponding to the appropriate colours in the linear spectrum between red and blue. Also shown in the figure are 4 × enlargements of the boundary layer near the entry corner of the warm wall. As either active wall has a similar influence on the interior fluid, it suffices to describe only the heated boundary region. A simple scale analysis is used to describe the early transient process. Implicit in the following scaling is the assumption that the dimensionless boundary-layer thickness δ is much less than unity for all values of t.

Initially, as can be observed from figure 3(*a*), heat is conducted from the hot wall, resulting in a heated layer next to the wall whose thickness grows as

$$\delta \sim t^{\frac{1}{2}}. \tag{3.1}$$

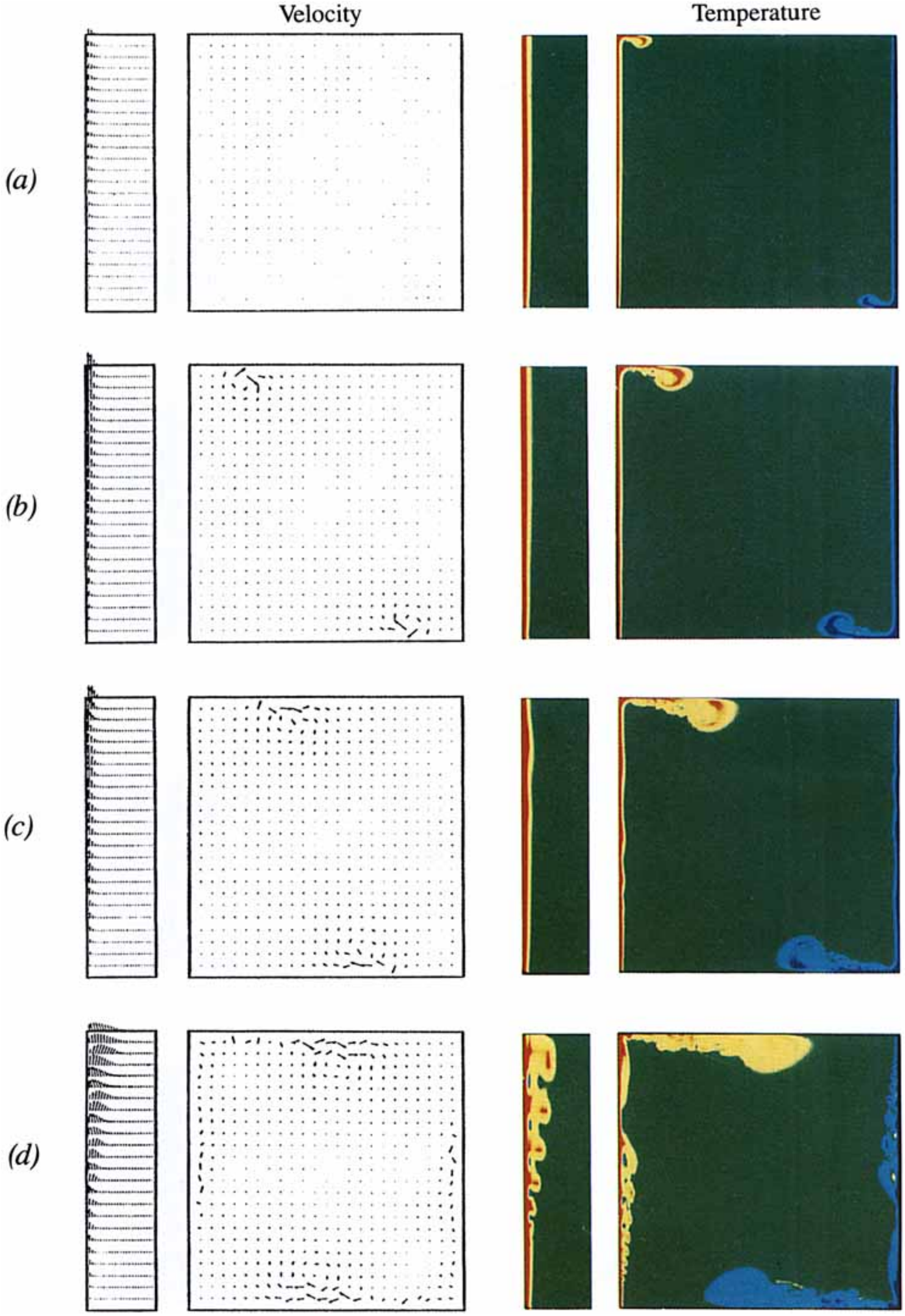

FIGURE 3 (*a-d*). For caption see Plate 3.

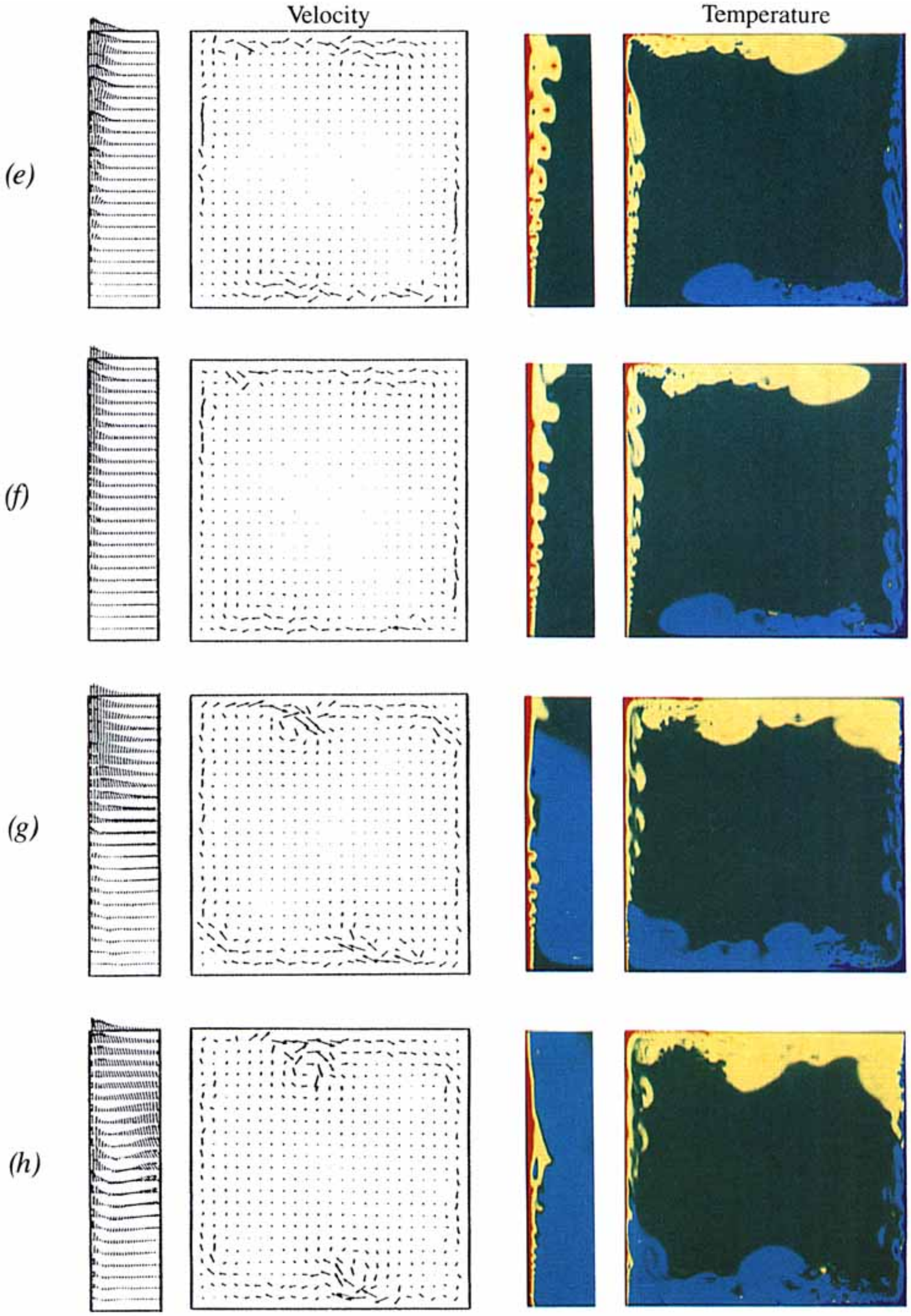

FIGURE 3 (*e-h*). For caption see Plate 3.

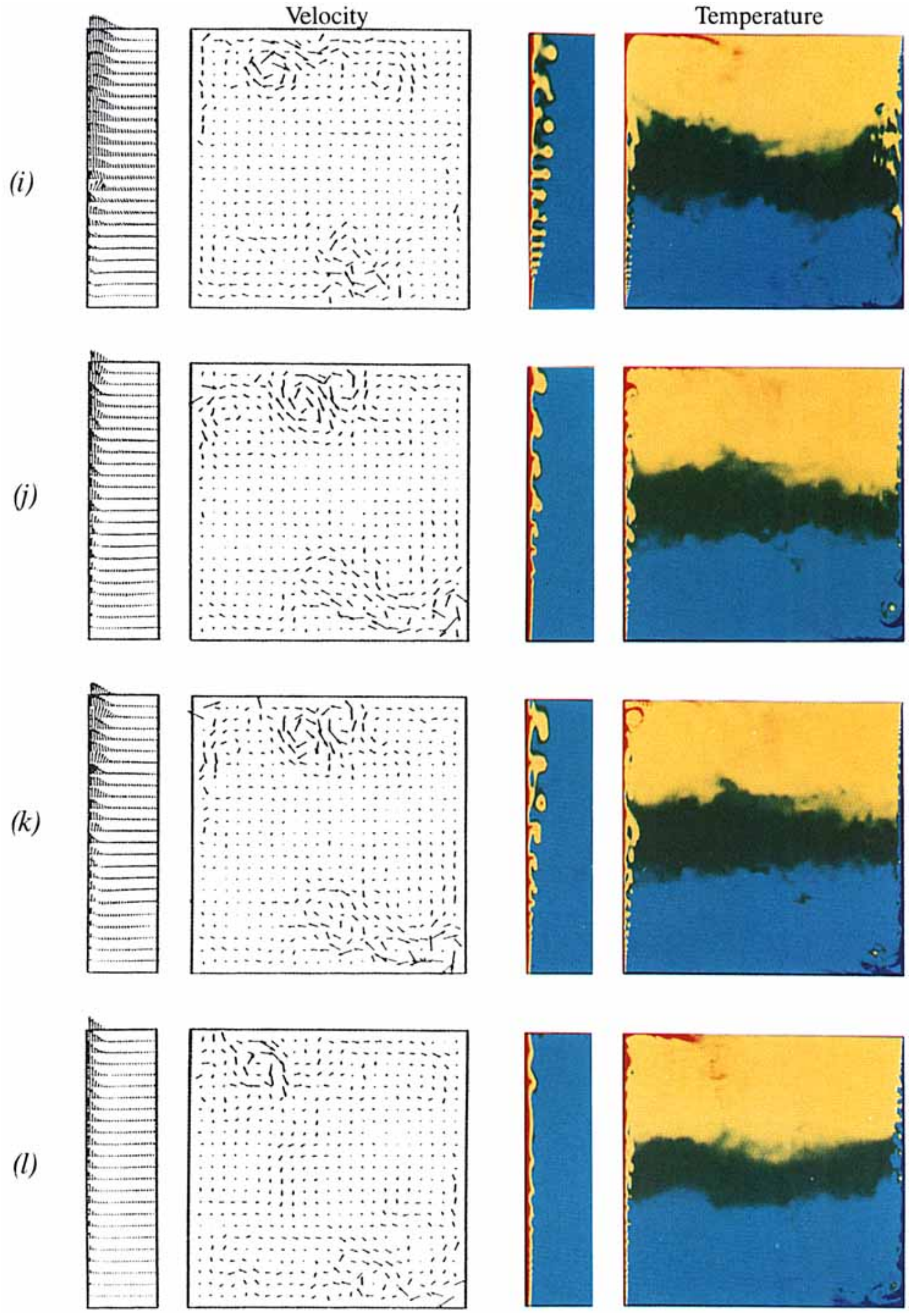

FIGURE 3. Velocity and temperature fields at selected instances: (*a*) $t = 3.10\times10^{-5}$, (*b*) 5.20×10^{-5}, (*c*) 8.07×10^{-5}, (*d*) 1.09×10^{-4}, (*e*) 1.22×10^{-4}, (*f*) 1.33×10^{-4}, (*g*) 1.61×10^{-4}, (*h*) 1.73×10^{-4}, (*i*) 6.58×10^{-4}, (*j*) 7.30×10^{-4}, (*k*) 7.40×10^{-4}, (*l*) 9.30×10^{-4}. Also shown are 4× enlargements of the boundary layer near the starting corner on the hot wall.

For $Pr < 1$, the resulting buoyancy forces, in balance with the unsteady inertial forces, act to accelerate this layer in the vertical direction with a velocity of

$$v \sim \tfrac{1}{2} Pr\, Ra\, t, \tag{3.2}$$

where the factor $\frac{1}{2}$ is introduced to account for the fact that at this time the temperature difference between the wall and the core of the cavity is only $\frac{1}{2}\Delta T$. Heat is also being convected vertically and the layer will continue to grow until the heat conducted in from the wall balances that convected away. This balance yields

$$\tau \sim \left(\frac{2A}{Pr\, Ra}\right)^{\frac{1}{2}} \tag{3.3}$$

as the growth time for the thermal boundary layer, at which time the length and velocity scales become

$$\delta \sim \left(\frac{2A}{Pr\, Ra}\right)^{\frac{1}{4}}, \tag{3.4}$$

and

$$v \sim (\tfrac{1}{2} A\, Pr\, Ra)^{\frac{1}{2}}, \tag{3.5}$$

respectively. The aspect ratio A is unity in our case.

The boundary layer on the hot wall is evidently unstable, and at $t \approx 1.4 \times 10^{-5}$ the first sign of an anomaly was detected in the thermal field at $y \approx 0.065$. Owing to the resolution of figure 3(*a*), this infinitesimal disturbance cannot be seen at $t = 3.10 \times 10^{-5}$; however, at $t = 5.20 \times 10^{-5}$ (figure 3*b*) one can observe a sinusoidal disturbance of small amplitude which has grown substantially by $t = 8.07 \times 10^{-5}$ (figure 3*c*). In figure 3(*d*) the waves begin to fold back in a distinctive 'hook' pattern, first observed by Elder (1965*b*) in a slot, and by Mordchelles-Regnier & Kaplan (1963) and Fujii *et al.* (1970) on a vertical surface. The ends of the hooks are eventually re-entrained by the boundary layer, and this folding process continues as the flow propagates from the bottom of the plate to the top. The first occurrence of wave folding is observed at $y \approx 0.21$, and it appears that full folding occurs by $y \approx 0.5$. This folding process can be observed from figure 3(*d*–*f*).

On closer examination, near the source of instability at $y \approx 0.065$, the critical wavenumber is found to be near 1.0–1.2×10^2 and the critical wave speed near 6.5×10^3. It is noted that both the wavelength and wave speed increase approximately linearly with distance up the plate. The observed values for the location of instability, and the critical wavenumber and wave speed are in good agreement with the respective values of 0.056, 97, and 7×10^3 obtained from a linear analysis by Tzuoo, Chen & Armaly (1985) for the semi-infinite vertical plate. The agreement is remarkable since in their case a leading edge is present at the bottom of the plate, so that the bottom boundary conditions are different.

Consider now the corner region where the rising flow is turned owing to the presence of the insulated top boundary. If we assume constant pressure where the rising flow is first turned, and use conservation of mass, it is possible to write a characteristic internal Froude number for the horizontal flow (see PC):

$$Fr = 0.125 A^{\frac{3}{8}} (Pr\, Ra)^{\frac{1}{8}}. \tag{3.6}$$

The flow is critical when $Fr = 1$. For $Fr > 1$ the flow is supercritical and may undergo an internal jump with an increase in depth of the flowing layer as it moves from supercritical to subcritical. As pointed out by Ivey (1984), by analogy with open-channel flow (Lighthill 1978), the energy loss associated with an internal jump is dissipated in a stationary wavetrain downstream of the jump for $1.0 < Fr < 1.3$, but for higher values of Froude numbers, these waves break, resulting in a disordered interface downstream. This scenario is consistent with the corner flow regions displayed in figure 3(*a–h*) as $Fr \approx 2.1$ in our case. It is noted that wave breaking is first observed in the computation at $t \approx 1.8 \times 10^{-5}$.

As time proceeds, from figures 3(*d*)–3(*f*) the boundary layers continue to break in a characteristic periodic pattern whose amplitude and wavelength remain approximately linear in y. In the meantime the heated and cooled intruding horizontal jets reach the opposing vertical walls at $t \approx 1.51 \times 10^{-4}$. As the cold jet impinges on the hot wall, we see from figure 3(*g*, *h*) that the previously established boundary-layer structure is destroyed. As more and more fluid is discharged into the core of the cavity, the fluid there is set into relatively weak motion and a stable vertical temperature stratification starts to become apparent in figure 3(*i–l*). As the thermal stratification is established, the internal jumps, previously present in the emerging corners, now become effectively flooded, in agreement with Ivey's observation. At this time, from figure 3(*i–l*), we also observe boundary layers having somewhat different structure than those present when the core was isothermal, but the presence of the hooks is still evident. As a wave propagates along the wall, a point is reached where a portion of the wave at the edge of the boundary layer is at a lower temperature than the interior of the boundary layer. It will thereby be decelerated and fall behind causing the characteristic hook. In figure 3(*j–l*) the flow approaches statistical steady state; however, we still observe periodic changes of the structure of the boundary layers, and intermittently the establishment of large coherent structures (as seen in figure 3*j*, *k*). A very peculiar result is that these coherent structures appear in pairs on the opposite walls. It is believed that this phase-locking mechanism can only be attributed to a characteristic dynamic pressure fluctuation which propagates through the cavity at infinite speed.

From the results we make the following observations regarding the stationary flow:

(*a*) Away from the walls the flow is fairly weak and the thermal field is stably stratified. The stratification is approximately linear, as seen from figure 4, with a slope of

$$\beta = \frac{A}{2\epsilon}\frac{\mathrm{d}\overline{T}}{\mathrm{d}y} = 0.38. \tag{3.7}$$

This result appears to be *independent* of Ra since it is in good agreement with the experimental results of Elder (1965*b*) who obtained $\beta = 0.3$–0.4 for $10 < A < 30$ and $Pr = 7$, Kutateladze *et al.* (1972*b*) who obtained $\beta = 0.33$ for $A = 22$ and $Pr = 13.2$, and Kutateladze *et al.* (1977, 1978) who obtained $\beta = 0.36 \pm 0.04$ for $8 < A < 26$, $Pr \approx 16$. The agreement is not as good when comparison is made with the experimental result of Cowan *et al.* (1982) who obtained $\beta = 0.54$ using water as the working fluid and $1.5 < A < 23$. This disagreement is easily explained by noting that their result was obtained by correlating data for $1.51 \times 10^{7} < Ra < 2.3 \times 10^{11}$. It is noted that the flow does not become fully turbulent until $Ra \approx 10^{9}$ and for lower values of Rayleigh number β is larger (see CP, and Kutateladze *et al.* 1978). Indeed, by considering only their data for $Ra = 2.26 \times 10^{11}$ and $A = 1.5$, a value of $\beta = 0.41$ is obtained, which is much closer to the result (3.7). A linear stratification is also known to occur in the laminar regime when Ra is large (see CP). That (3.7) is independent of the Prandtl number is not very surprising since Elder (1965*a*), in comparing laminar results for $Pr = 0.7$–10^{3}, concluded that at best β is a weak function of Pr.

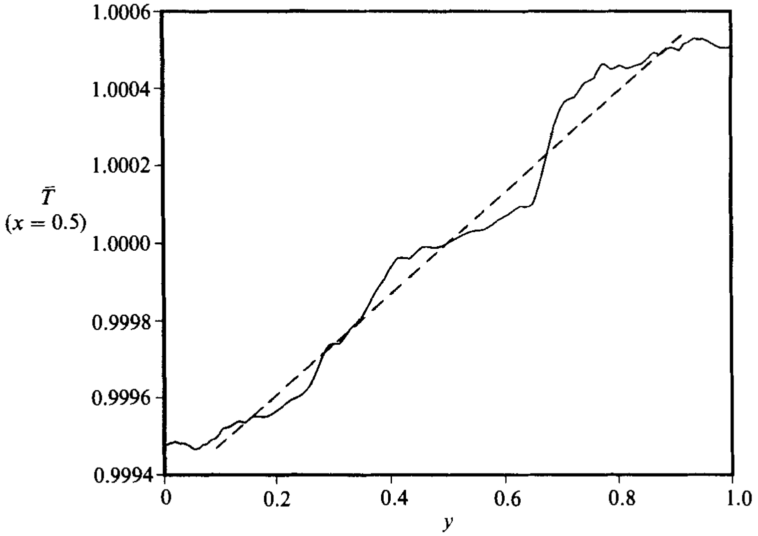

FIGURE 4. Mean temperature distribution at the mid-width of the cavity. The dashed line represents a linear approximation.

In the turbulent case it is expected that any Prandtl-number dependence would become even less important. What is surprising is that in strong turbulence β is independent of the Rayleigh number.

(*b*) Prominent features of the boundary layers are hook-like structures similar to the ones reported by Elder (1965*b*) in his experiments with water, and by Fujii *et al.* (1970) in spindle oil. The initial oscillations grow in amplitude as they propagate along the plate. The outer portion of the waves, which are in a region of slower moving fluid, curl over and, relative to the head of the wave front, are left behind. However, owing to a lower pressure behind the waves, these hook-like structures are re-entrained at the tail end, along with fluid from the interior, thus initiating a folding process which continues as the waves propagate along the plate. This process is disrupted when the vorticity within these structures becomes too large, causing them to break up. In figure 3(*k*) we clearly see this folding process occurring near $y = 0.5$ on the hot plate. This scenario is in complete agreement with the detailed photographs shown in figure 16 of Fujii *et al.* (1970).

(*c*) Occasionally, a pair of vortices are generated (one on each active wall) which do not break up and are seen as very intense vortex rolls as they convect along the walls. These rolls, after negotiating the departing corners, are quickly diffused. In figure 3(*k*) we can see a pair of fully developed vortices about to be discharged into the core of the cavity.

3.2. *Heat Transfer*

A different perspective on the early transient flow is obtained by looking at figure 5, where the spatially averaged Nusselt numbers $\langle Nu_h \rangle$ and $\langle Nu_c \rangle$ on each of the active walls are displayed together with their sum $\langle Nu_0 \rangle$ (note that $\langle Nu_c \rangle$ is negative since heat flows out at the cold wall). The brackets $\langle \ldots \rangle$ denote averaging over the y-direction. By looking at the record of $\langle Nu_h \rangle$ we observe that until $t \approx 1.4 \times 10^{-5}$, which corresponds to the first observation of a perturbation in the boundary layer, the heat transfer is through conduction and decays as $t^{-\frac{1}{2}}$ as expected. At $t \approx 3.1 \times 10^{-5}$ the heat conducted in from the wall is balanced by that convected away

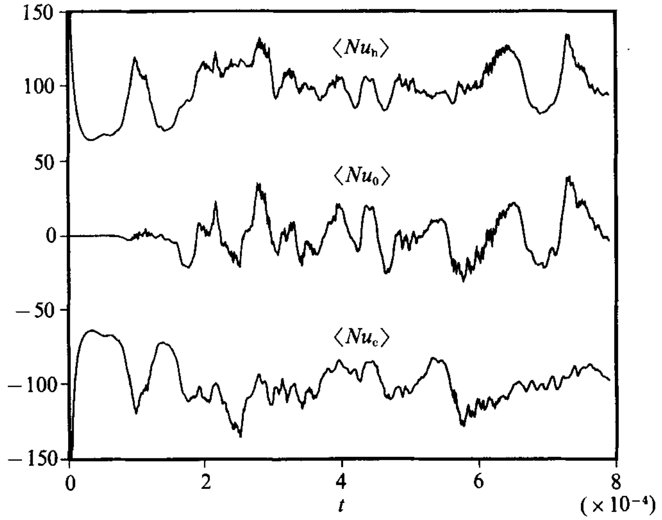

FIGURE 5. Average Nusselt numbers $\langle Nu_h \rangle$ and $\langle Nu_c \rangle$ on the active walls, and their sum $\langle Nu_0 \rangle$ as functions of time.

by buoyancy as manifested by a minimum in the heat transfer rate there. During the period of time from $t \approx 3.1 \times 10^{-5}$ to $t \approx 8 \times 10^{-5}$, which corresponds to the period of time when the perturbation on the boundary layer is sinusoidal and of small amplitude, the heat transfer rate increases slightly. However, for $t \approx 0.8\text{–}1.0 \times 10^{-4}$ we observe an approximately linear increase in $\langle Nu_h \rangle$ during which time the amplitudes of the disturbances grow to a finite size. The peak in heat transfer near $t \approx 1.0 \times 10^{-4}$ corresponds to the beginning of the wave-folding and breaking process. We note that for $t > 1.0 \times 10^{-4}$ the heat transfer on the two active walls is unequal and becomes more so as time proceeds as evidenced by the record of $\langle Nu_0 \rangle$.

For Rayleigh numbers in the turbulent regime, it is well known that the average Nusselt number at a heated wall obeys the relation (e.g. Goldstein 1938; Jakob 1949; Elder 1965*b*)

$$\overline{\langle Nu \rangle} = C Ra^{\frac{1}{3}}. \tag{3.8}$$

Expression (3.8) follows from the fact that since the boundary-layer thickness is much smaller than the width of the cavity, the heat transfer should be independent of L. When the computed flow becomes stationary, the following values of average Nusselt numbers and r.m.s. fluctuations are obtained (see figure 5): $\overline{\langle Nu_h \rangle} = 99.54$, $\overline{\langle Nu_c \rangle} = -98.96$, $\overline{\langle Nu_0 \rangle} = 0.59$, and $\sigma_{Nu_h} = 10.02$, $\sigma_{Nu_c} = 10.70$, $\sigma_{Nu_0} = 15.63$. Two points are worth noting. First, the relatively small value of $\overline{\langle Nu_0 \rangle}$ indicates that the heat transfer is stationary to within 0.6%, since ideally we would then expect $\overline{\langle Nu_h \rangle} = -\overline{\langle Nu_c \rangle}$ and $\overline{\langle Nu_0 \rangle} = 0$. Second, the r.m.s. fluctuations are of the order of 10%, and their timescales are relatively long (see figure 5). If the average Nusselt number between the two active walls is taken to be $\overline{\langle Nu \rangle} = 99.25$, from (3.8) we obtain 0.046 for the constant C. This value is compared in table 1 with experimental values obtained by the authors indicated. The agreement with the experimental values is excellent, and, as with the value of β in (3.7), the constant C appears to be independent of the Prandtl number and aspect ratio, since the experimental results were obtained for $1 \leqslant Pr \leqslant 10^3$ over the aspect ratio range $1 < A < 61$.

As first pointed out by Eckert & Carlson (1961), and more recently by Kutateladze

Investigator	C	C'	C_1	C_2	C_3	C_4	C_5	C_6	Comments
Vertical cavity:									
Present work	0.046	0.106 (0.115)	0.118	2.406	0.943	3.89	13.63	8.77	$Pr = 0.71$, $A = 1$
Elder (1965*b*)	0.053 ± 6 %	—	0.00467	7.69	1.08	—	—	—	$Pr \approx 7$, 10^3, $A = 10$–30
MacGregor & Emery (1969)	0.046	—	—	—	—	—	—	—	$Pr = 1$–20, $A = 10$–40
Kutateladze *et al.* (1977)	—	0.108 (0.098)	0.0388	—	—	—	—	—	$Pr \approx 16$, $A = 8$–26
Cowan *et al.* (1982)	0.043	—	—	—	—	—	—	—	Water, $A = 1.5$–61
Kirdyashkin *et al.* (1983)	—	(0.112)	0.0491	3.125	0.906	—	—	—	$Pr \approx 12$, $A = 11.2$
Vertical plate:									
Pirovano *et al.* (1970)	—	0.10	—	—	—	—	—	—	N_2 and CO_2
Kutateladze *et al.* (1975)	—	—	—	—	—	20.3	—	—	$Pr \approx 16$
George & Capp (1979)	—	0.13	0.1	1.45	0.35	—	12.3	9.3	Air
Cheesewright & Ierokiopitis (1982)	—	0.13	—	—	—	—	—	—	Air
Siebers *et al.* (1985)	—	0.110	0.127	1.42	0.36	—	—	—	Air

TABLE 1. Comparison of values in equations (3.8), (3.9), (3.12), (3.15), (3.18), and (3.19) with those obtained from results of other investigators.

et al. (1977), the heat flux on the hot wall decreases with increasing longitudinal coordinate; however, the dependence of the dimensionless heat transfer coefficient $\overline{Nu}_y$ on the Rayleigh number Ra_y, where both parameters are based on $\Delta T_{\mathrm{m}} = T_{\mathrm{h}} - \overline{T}_{\mathrm{m}}$, is the same as that for turbulent natural convection near an isothermal vertical plate:

$$\overline{Nu}_y = C' Ra_y^{\frac{1}{3}}. \tag{3.9}$$

Note that while in the case of an isolated vertical plate $\overline{T}_{\mathrm{m}}$ is the constant ambient temperature, in the cavity it is a function of the vertical coordinate. It appears that, away from the cavity ends, since ΔT_{m} also decreases with increasing longitudinal coordinate, the inner structure of the thermal boundary layer at any fixed y is locally similar to that of an isolated plate. More will be said about this in the following section. The value of C' obtained from the simulation is 0.106 and is noted in table 1 along with values obtained by others. It is noted that George & Capp (1979) obtained a value of C' from a scale analysis in conjunction with experimental data by others, while Kutateladze *et al.* (1977) obtained C' from experimental results in a differentially heated cavity. The values in parentheses attributed to Kutateladze *et al.* (1977), and Kirdyashkin *et al.* (1983), were obtained by the present author by differentiating their temperature distributions near the wall. All other values of C' were obtained experimentally from an isolated vertical plate. It is evident from the table that the result for C' is in general agreement with previously known values.

To test the consistency of the calculations, we can approximate the temperature at the mid-width of the cavity, away from the ends, by the equation (see figure 4)

$$\frac{\Delta T_{\mathrm{m}}}{\Delta T} = 0.690 - 0.379y. \tag{3.10}$$

Following Eckert & Carlson (1961) (3.9) can be integrated to obtain the average Nusselt number in the form (3.8). The result of such calculation yields $C' = 0.115$ if $C = 0.046$ is assumed to be accurate. This value appears in parentheses in table 1. The slight variation between the two computed values of C' is expected since the temperature in the core was modelled with (3.10), and since some scatter also existed in the variation of $\overline{Nu}_y$ with Ra_y.

3.3. *Mean temperature and velocity*

Figures 6 and 7 show the mean temperature and velocity distributions at the mid-height of the cavity. In each of the figures the distribution across the cavity, and details near the hot wall are shown. Figures 6(*a*) and 7(*a*) reveal that large horizontal gradients exist in the boundary-layer regions but, as noted before, outside these, the horizontal gradients are essentially zero. Although not shown, we point out the presence of a very weak horizontal flow (due to entrainment by the boundary layers) whose sign is opposite to that of the vertical velocity, and whose average magnitude reaches an extremum near the exterior edge of the boundary layer of approximately 3% of the maximum vertical velocity. The results are in agreement with Elder's (1965*b*) observation that the turbulent interior is a region of uniform mean temperature and zero mean velocity. The boundary layer region is shown in greater detail in figures 6(*b*) and 7(*b*). As can be seen from the figures, the boundary layers on the active walls are very thin at this high Rayleigh number, thus causing the problem to become stiff owing to the disparate lengthscales present. Upon making detailed comparisons with the corresponding laminar boundary layer, one further

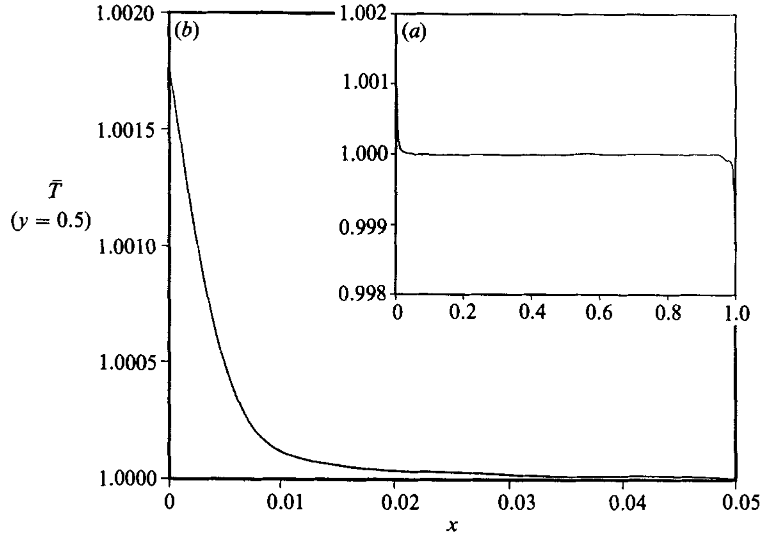

FIGURE 6. Mean temperature distribution at the mid-height of the cavity: (*a*) complete distribution, (*b*) detail of the hot wall boundary layer.

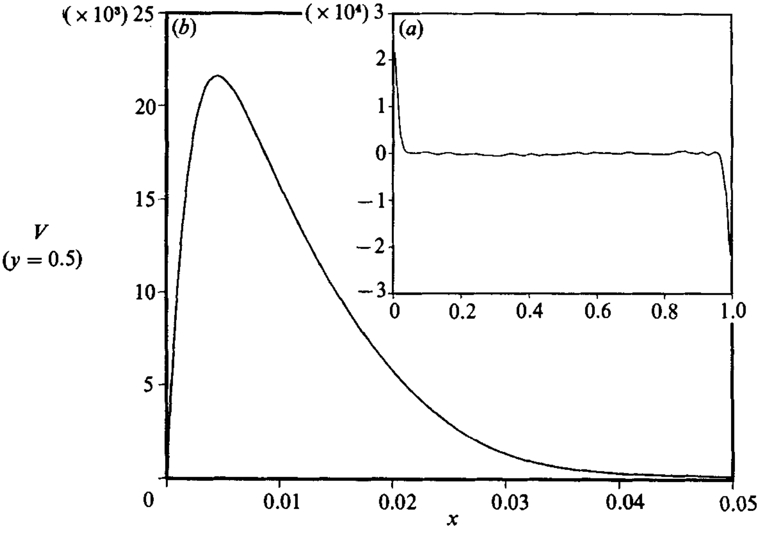

FIGURE 7. Distribution of mean vertical velocity component at the mid-height of the cavity: (*a*) complete distribution, (*b*) detail of the hot wall boundary layer.

notes that the distributions in figures 6(*b*) and 7(*b*) are broader, especially in the exterior part of the layer. We shall elaborate upon this aspect later in the paper.

Even though the time-averaged boundary-layer distributions of temperature and velocity are very smooth and well behaved, large fluctuations occur there. In figure 8 small samples of temperature and velocity records are shown at six selected locations on the cavity mid-height. From the figure a few observations can be made. First, we note that well inside the boundary layer T and v are well correlated. Second, while the fluctuations of v are much larger than those of u well inside the boundary layer, the opposite occurs near the edge. This result is a direct consequence of the presence of a stable stratification in the core of the cavity which resists vertical

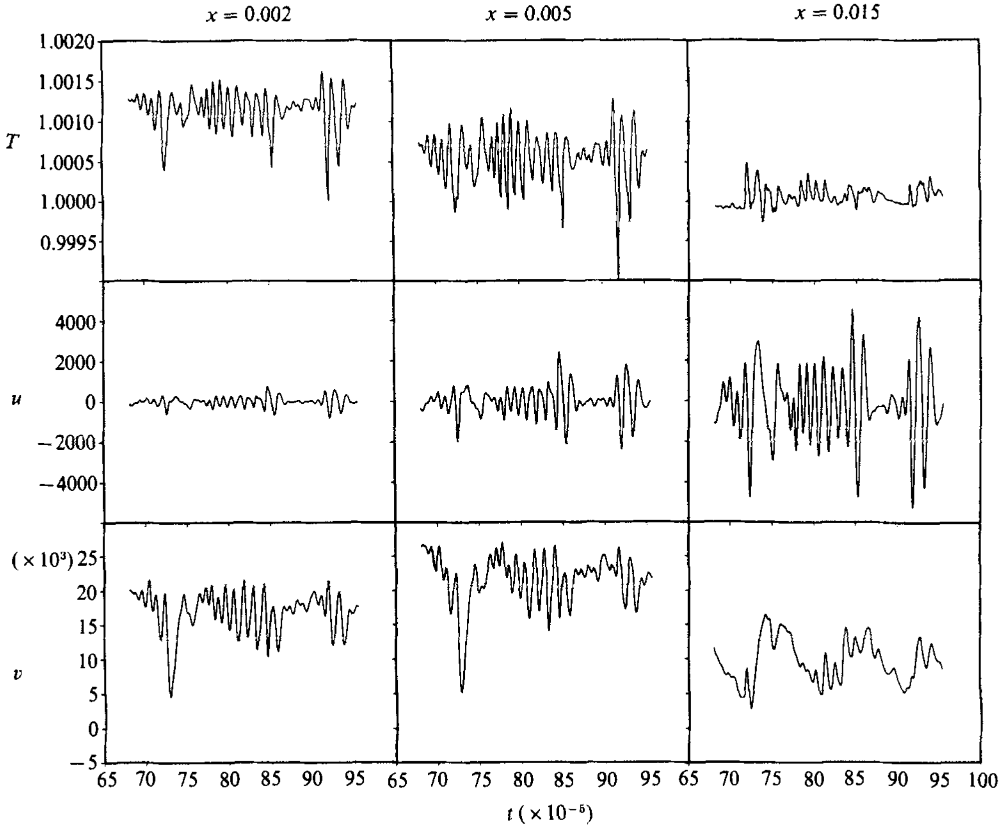

FIGURE 8. For caption see facing page.

motion. Also note the intermittent character of T and v at the edge of the layer. Lastly, we note that the time samples shown in figures 5 and 8 include time values of the temperature and velocity fields in figure 3 (j–l). The large fluctuations caused by the large structure, noted in figure 3 (j, k), can be clearly seen in figures 5 and 8 near $t \approx 7.4 \times 10^{-4}$. Note that its influence extends to the edge of the velocity boundary layer. The samples shown in figure 8 have similar characteristics to those observed by Kirdyashkin *et al.* (1983) in a cavity for $Pr \approx 12$, and by Fujii *et al.* (1970) on a vertical surface for $Pr = 69$.

Eckert & Carlson (1961), and Kutateladze *et al.* (1977) noted that the inner structure of the thermal boundary layer is locally similar to that of an isolated plate. More recently, George & Capp (1979), using classical scaling arguments, presented a theory for turbulent natural-convection boundary layers next to heated vertical surfaces. They showed that the boundary layer must be treated in two parts: an outer region, in which the viscous and conduction effects are negligible, and an inner region, in which the mean convection terms are negligible. The inner layer, which is identified as a constant heat flux layer in the sense that the total heat flux across the layer is independent of the distance from the wall, consists of two regions: a conductive and viscous sublayer, in which the temperature is linear and the velocity approximately linear next to the wall; and a buoyant sublayer outside of it, where the mean velocity and temperature profiles depend on the cube root and inverse cube root of distance from the wall, respectively. In figures 9 and 10 the computed mean

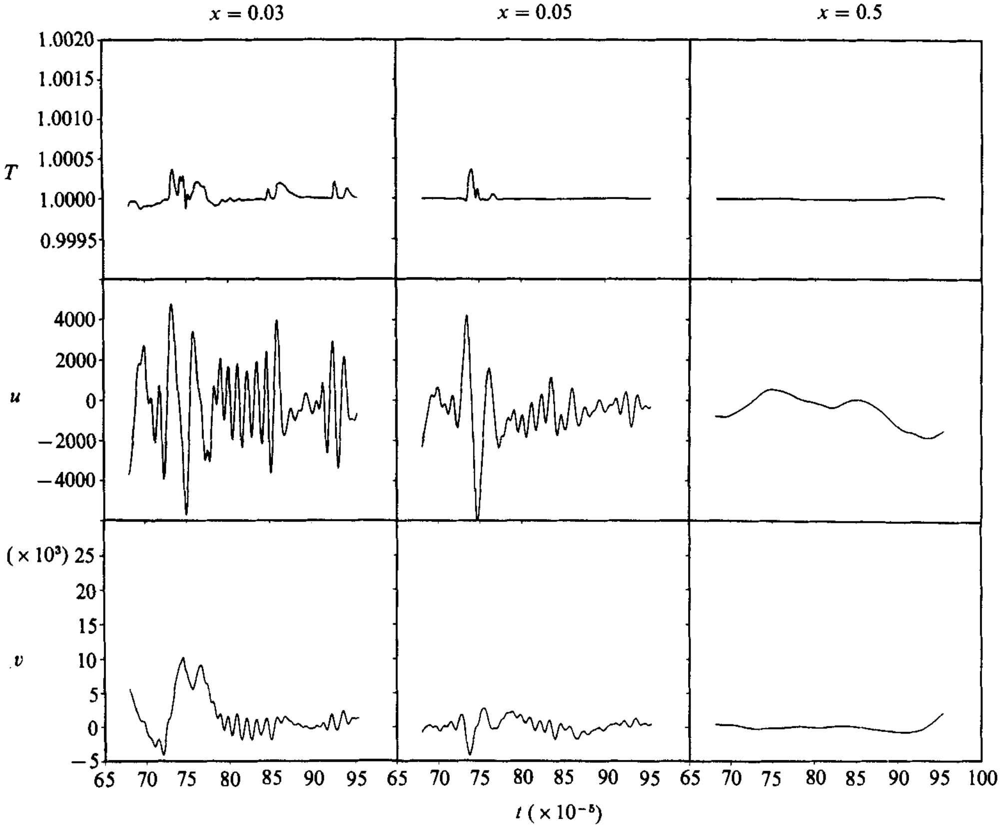

FIGURE 8. Time histories of T, u, and v obtained from the mid-height of the cavity at x-locations labelled on the figure.

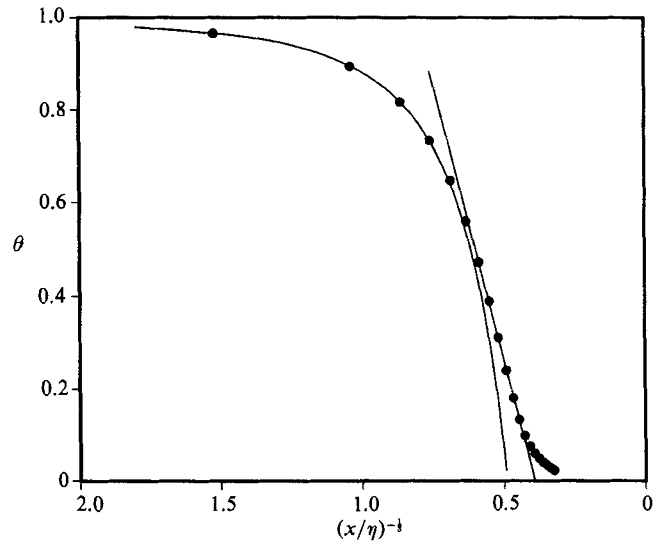

FIGURE 9. Plot of mean temperature at the mid-height of the cavity in the vicinity of the hot wall; θ is defined by (3.11). The lines correspond to (3.12) and (3.15) with the constants reported in table 1, while the points denote the computed mean temperature at their respective grid location.

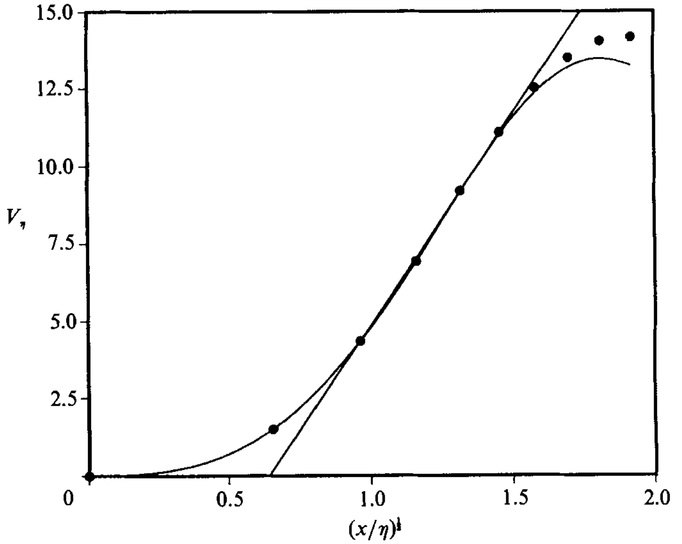

FIGURE 10. Plot of mean vertical velocity component at the mid-height of the cavity in the vicinity of the hot wall; V_η is defined by (3.11). The lines correspond to (3.18) and (3.19) with the constants reported in table 1, while the points denote the computed mean velocity at their respective grid location.

temperature and velocity distributions, $\bar{T}$ and V respectively, are plotted in the inner region at the mid-height of the cavity using the following scales:

$$\theta = \frac{\bar{T}-\bar{T}_m}{T_h-\bar{T}_m}, \quad V_\eta = \eta V, \tag{3.11}$$

where $\eta = (\beta g \Delta T_m L^3/\alpha^2)^{-\frac{1}{3}}$ is the dimensionless thermal (inner) lengthscale. Note that T_h and $\bar{T}_m$ are dimensionless in (3.11) and, because of symmetry, $\bar{T}_m = 1$ and $\eta = (\frac{1}{2}Pr\,Ra)^{-\frac{1}{3}}$ at the cavity mid-height. The symbols in the figures represent computed grid locations, while the curves represent best fits of the numerical data using the functional forms suggested by George & Capp. Values of constants $C_i, i = 1, \ldots, 6$, presented below are recorded collectively in table 1 together with those that the present author was able to extract from the experimental works listed in the table. The exceptions are the results of George & Capp (1979), where they themselves obtain the constants using experimental data of Cheesewright (1968), Fujii *et al.* (1970), and Smith (1972). From figure 9 we see that in the range $0 \leqslant x/\eta < r_1^\theta$ a uniform mean temperature distribution corresponding to the linear equation

$$\theta = 1 - C_1\left(\frac{x}{\eta}\right) \tag{3.12}$$

is obtained with $C_1 = 0.118$. This region is the conductive sublayer. Using a simple analysis along with their experimental data and that of Cheesewright (1968), Kutateladze, Kirdyashkin & Ivakin (1975) show that the conductive sublayer should extend through

$$r_1^\theta = 3.91 Pr^{\frac{1}{2}}. \tag{3.13}$$

The resulting estimate for the range is in excellent agreement with our result of 3.3 for $Pr = 0.71$, and Elder's (1965*b*) estimate of 137 for $Pr \approx 10^3$. The constant C_1 is a direct measure of the heat flux at the wall. Indeed it can be easily shown that if C' is universal (as the data in table 1 indicate), then using (3.9) with (3.12) the following Prandtl number dependence for C_1 is obtained:

$$C_1 = C' Pr^{-\frac{1}{3}}. \tag{3.14}$$

If the value of $C' = 0.106$ is used, then the value of C_1 resulting from (3.14) is in good agreement with those listed in the table, with the exception of the value obtained from Elder's data which is approximately a factor of two smaller. It is not clear what the reason is for this large discrepancy; however, Kirdyashkin *et al.* (1983) very clearly show that substantially lower values of C' could result for Rayleigh numbers in the transition regime. Additionally, the Prandtl number used in Elder's experiment is not known very accurately.

Outside the sublayer, in the mixing region, the thermal field has the following behaviour:

$$\theta = C_2\left(\frac{x}{\eta}\right)^{-\frac{1}{3}} - C_3, \tag{3.15}$$

which is accurate in the range $r_1^{\theta} < x/\eta < r_2^{\theta}$ with $C_2 = 2.406$, $C_3 = 0.943$, and $r_2^{\theta} = 13$. Using our result along with Elder's (1965*b*) experimental result for $Pr \approx 10^3$ the following estimate for the external edge of the boundary layer is obtained:

$$r_2^{\theta} = 15.43 Pr^{\frac{1}{2}}. \tag{3.16}$$

George & Capp (1979) conclude that C_2 is a function of Prandtl number while C_3 is a universal function. The Prandtl-number dependence of C_2 appears to be weak; indeed using our data with those of Elder (1965*b*) and Kirdyashkin *et al.* (1983) we obtain

$$C_2 = 2.35 Pr^{\frac{1}{6}}. \tag{3.17}$$

In addition, as noted from table 1, it appears that the value of the 'universal' constant C_3 in the cavity is approximately a factor of three larger than that for an isolated plate. This difference must be attributed to the presence of a stable stratification exterior to the mixing layer which was not accounted for by George & Capp. Note that the value of C_3 obtained from the data of Kirdyashkin *et al.* (1983) for $Pr \approx 12$ and Elder (1965*b*) for $Pr \approx 10^3$, differ by 4% and 15%, respectively, from our value obtained for $Pr = 0.71$.

As can be seen from figures 9 and 10, the conductive sublayer encompasses both the viscous sublayer, approximately given by

$$V_\eta = Pr^{-1}\left[C_4\left(\frac{x}{\eta}\right) - \frac{1}{2}\left(\frac{x}{\eta}\right)^2 + \frac{C_1}{6}\left(\frac{x}{\eta}\right)^3\right] \tag{3.18}$$

with $C_4 = 3.89$ and valid in the range $0 \leqslant x/\eta < r_1^V$ with $r_1^V = 1.5$, and the momentum buoyant sublayer given by

$$V_\eta = C_5\left(\frac{x}{\eta}\right)^{\frac{1}{3}} - C_6, \tag{3.19}$$

with $C_5 = 13.63$ and $C_6 = 8.77$ in the range $r_1^V < x/\eta < r_2^V$, where $r_2^V = 3.3$. The constant $C_4 = \tau_w/\rho(\beta g \Delta T_m \alpha)^{\frac{2}{3}}$ represents the friction coefficient and is expected to be a function of the Prandtl number. For an isolated vertical plate and $Pr \approx 16$, Kutateladze *et al.* (1975) used their results and those of Cheesewright (1968) to obtain the following Prandtl-number dependence:

$$C_4 = 5.2 Pr^{\frac{1}{2}}. \tag{3.20}$$

The value of C_4 obtained in the numerical simulation (see table 1) differs by approximately 13% from the result obtained from (3.20). In the momentum buoyant sublayer George & Capp (1979) note that C_5 should depend on the Prandtl number, while C_6 is expected to be a 'universal' function. We are unable to provide an estimate for the Prandtl-number dependence on C_5 owing to lack of data for fluids with Prandtl number larger than unity; however, it is expected that C_6 should depend on the stratification. We point out, however, that values of C_5 and C_6 obtained from the simulation are in good agreement with those reported by George & Capp for an isolated plate, thus indicating that the dependence on the stratification of C_6 is weak. Since the momentum buoyant sublayer is inside the conductive sublayer, it is not affected by the stable stratification present in the core of the cavity. Because of this stabilizing effect, the conductive sublayer extends approximately three times further from the wall than in the case where the stratification is absent. Thus, while the thickness of the conductive and viscous sublayers, and the thermal and momentum buoyant sublayers coincided in the isolated vertical plate, they do not in the vertical cavity, owing to the presence of a stable stratification in the core. However, in both cases the viscous sublayer extends to approximately the same distance from the wall (George & Capp report $r_1^V = 1.7$). We remark that the distributions (3.12) and (3.18) are the same as those derived from an asymptotic analysis of the turbulent boundary layer by Plumb (1976). Finally, we note that while it is possible to find logarithmic regions in the buoyant sublayers, the $-\frac{1}{3}$ and $+\frac{1}{3}$ distributions given by (3.15) and (3.19) fit the numerical results better and hold over a larger region.

As a direct result of the mixing outside of the viscous sublayer, the location of the velocity maximum $x_{\mathrm{M}} = 4.649 \times 10^{-3}$, and the momentum boundary-layer thickness $\delta_V = \int_0^{\frac{1}{2}} (V/V_{\mathrm{M}})\,\mathrm{d}x = 1.214 \times 10^{-2}$, are approximately 18% and 40% larger than the corresponding laminar ones, given by $x_{\mathrm{M}} = 1.3(A\,Pr/Ra)^{\frac{1}{4}}$ and $\delta_V = 2.1(A/Pr\,Ra)^{\frac{1}{4}}$ (see CP and PC). However, the velocity maximum $V_{\mathrm{M}} = 2.159 \times 10^4$ is still predicted within 1.5% by the correlation

$$V_{\mathrm{M}} = 0.26(A\,Pr\,Ra)^{\frac{1}{2}} \tag{3.21}$$

which is valid in the laminar regime! Using experimental results for the vertical flat plate for $0.7 \leqslant Pr \leqslant 17$, and for the vertical slot for $Pr \approx 16$, Kutateladze *et al.* (1972*a*, *b*) obtained the behaviour of the product $V_{\mathrm{M}}\,x_{\mathrm{M}}$ as a function of the Prandtl number and the stratification exterior to the boundary layer. Their results can be combined and recast in the form

$$V_{\mathrm{M}}\,x_{\mathrm{M}} \approx 200Pr^{\frac{1}{2}}(1-1.0\beta-0.8\beta^2), \tag{3.22}$$

where β is defined by (3.7). Using the above equation with (3.21), x_{M} can be estimated. The resulting value is found to be within 17% of the value obtained numerically.

As suggested by George & Capp (1979) for the isolated vertical plate, and Kutateladze *et al.* (1977) for the vertical slot, the vertical velocity distribution exterior to the maximum should only scale with the boundary-layer thickness

$$\frac{V}{V_{\mathrm{M}}} = f_V\left(\frac{x}{\delta_V}\right), \tag{3.23}$$

although the distribution is expected to be different in the two cases. In figure 11 such a distribution obtained from the numerical simulation is compared with

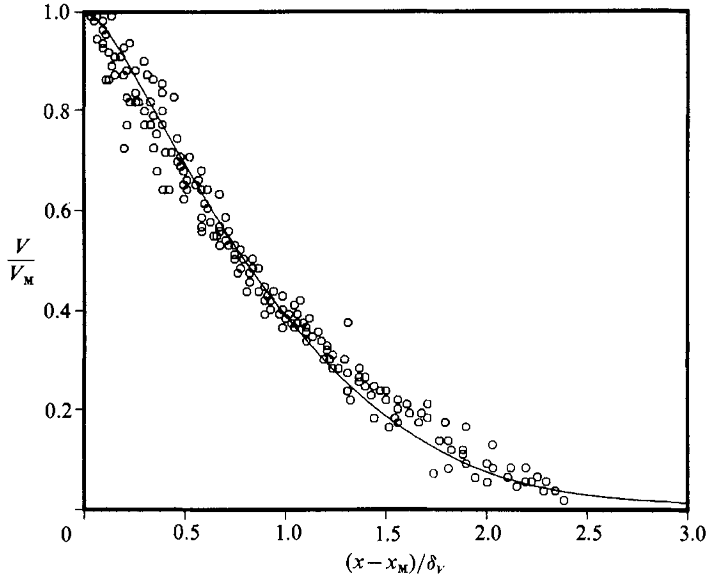

FIGURE 11. Mid-height vertical velocity distribution exterior to the maximum. The line is the result of the simulation, while the symbols are experimental results of Kutateladze *et al.* (1977).

experimental data obtained by Kutateladze *et al.* (1977) for $8 \leqslant A \leqslant 26$ and $Pr \approx 16$. As can be observed from the figure, the agreement is good. Furthermore, we note that since the data of Kutateladze *et al.* were obtained at different vertical locations for the different aspect ratios, the velocity profiles in the outer part of the boundary layer are self-similar in the above coordinates. From the numerical results we find that the distribution is approximated by

$$f_V = \exp\left[-0.947\left(\frac{x}{\delta_V}\right)^{1.432}\right], \tag{3.24}$$

with a correlation coefficient of 0.9994. George & Capp (1979) also theorized that the temperature profile in the outer region of the boundary layer depends on the same scaling. However, such a region, if it exists, must be very small in our case since the temperature at the edge of the $-\frac{1}{3}$ region is already very near to the core value of unity. This difference is attributed to the presence of a stable stratification in the core of the cavity, since in the vertical flat plate $\theta \approx 0.2$ at the edge of the boundary layer (see Siebers *et al.* 1985).

3.4. *Correlations and r.m.s. fluctuations*

The intensities of velocity and temperature fluctuations in the hot-wall boundary-layer region at $y = \frac{1}{2}A$ are shown in figures 12 and 13 using different scales. From figure 12 we see that near the wall the fluctuations are highly damped and approach zero on the wall itself (note that $(\overline{\theta'^2})^{\frac{1}{2}} = (\overline{T'^2})^{\frac{1}{2}}/\Delta T_m$). In fact from figure 13 we observe that in the vicinity of the wall the r.m.s. temperature and vertical velocity fluctuations approach zero at rates of 2.5 and 5.5 times faster than those of the respective averages. The rate of decay of the vertical velocity fluctuations near the wall is in good agreement with the experimental result $(\overline{v'^2})^{\frac{1}{2}}/V \approx 0.2$ obtained by Cheesewright & Ierokiopitis (1982) from an isolated vertical plate immersed in air. Furthermore, Kirdyashkin *et al.* (1983) obtain $(\overline{\theta'^2})^{\frac{1}{2}}/(1-\theta) \approx 0.3$ for the rate of decay

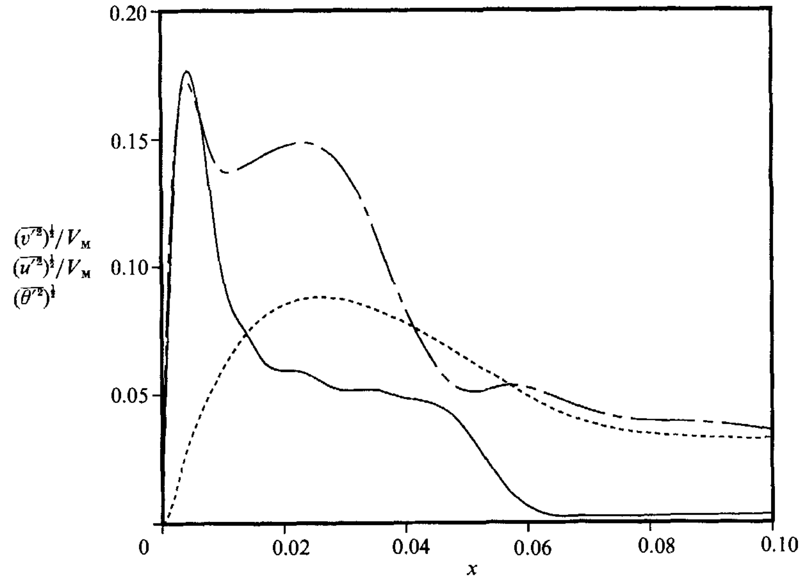

FIGURE 12. Distributions of turbulent r.m.s. fluctuations at the mid-height of the cavity and in the vicinity of the hot wall: ————, $(\overline{\theta'^2})^{\frac{1}{2}}$; – – – –, $(\overline{u'^2})^{\frac{1}{2}}/V_M$; - - - - - - - -, $(\overline{v'^2})^{\frac{1}{2}}/V_M$.

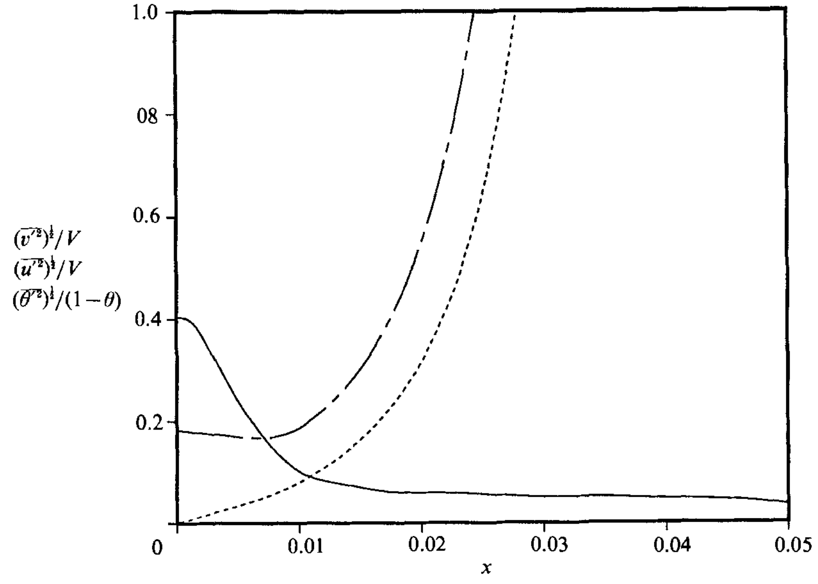

FIGURE 13. Distributions of turbulent r.m.s. fluctuations at the mid-height of the cavity and in the vicinity of the hot wall: ————, $(\overline{\theta'^2})^{\frac{1}{2}}/(1-\theta)$; – – – –, $(\overline{u'^2})^{\frac{1}{2}}/V$; - - - - - - - -, $(\overline{v'^2})^{\frac{1}{2}}/V$.

of temperature fluctuations near the wall of their cavity, and observe that the rate of fluctuations drop off monotonically away from the wall, in qualitatite agreement with figure 13. We observe that the quantitative difference between their result of 0.3 and our result of 0.4 is due to the difference in our respective Prandtl numbers.

As we move away from the wall, the fluctuations increase sharply until, as shown in figure 12, they reach a maximum near x_M where the mean vertical velocity is a maximum (see figure 7). There, the amplitude of the temperature and vertical

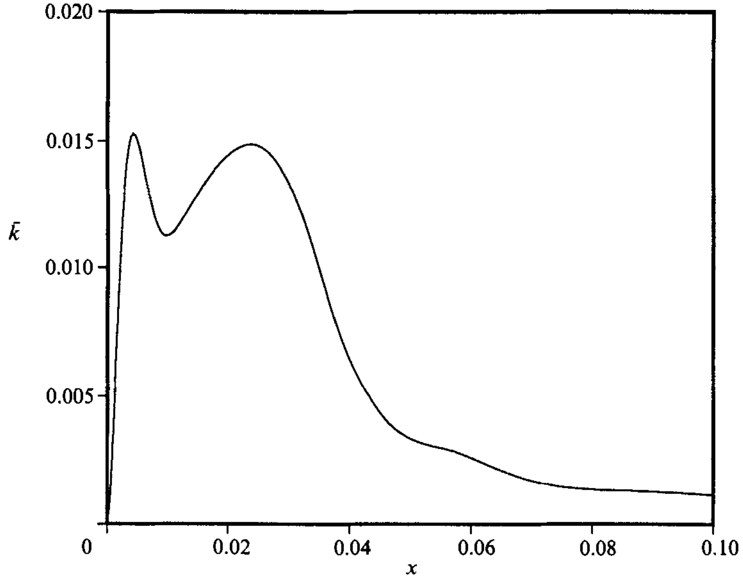

FIGURE 14. Distribution of mean turbulent kinetic energy at the mid-height of the cavity and in the vicinity of the hot wall.

velocity fluctuations are approximately 18% and 17% of the average values, respectively. The magnitude of the maximum temperature fluctuations and its location relative to the wall are in good agreement with the experimental results of Kutateladze *et al.* (1977, 1978) and Kirdyashkin *et al.* (1983) who, using 96% ethyl alcohol as the working fluid in a slot of aspect ratio 11.3, obtained a maximum of approximately 16% near $x \approx 5 \times 10^{-3}$. However, their maximum r.m.s. fluctuations for the vertical velocity component is approximately 35%, which is much greater than ours, and occurs near the location of their maximum velocity (consistent with our observation), which is approximately twice as far from the wall as their location of maximum temperature fluctuations. The difference in our results can be explained if the thickness of the viscous sublayer r_1^V (and subsequently r_2^V) is a stronger function of Prandtl number than the thickness of the conductive sublayer r_1^θ which increases with $Pr^{\frac{1}{2}}$. Unfortunately, no data are available to estimate the Prandtl-number dependence of r_1^V.

Moving further away from the wall to the edge of the boundary layer, we note from figure 12 a local maximum of approximately 15% in the r.m.s. fluctuations of the vertical velocity. From the figure we observe that the location of this maximum at $x \approx 0.0263$ coincides with a corresponding maximum of approximately 9% in the horizontal velocity fluctuations. The high intensity of velocity fluctuations in this region indicates that a high degree of mixing occurs. Thus, it appears that most of the mixing occurs at the exterior edge of the boundary layer. The presence of the two maxima is also apparent in figure 14 where the mean turbulent kinetic energy $\bar{k} = \frac{1}{2}\overline{u_i' u_i'}$ is plotted as a function of x. This outer mixing region isolates the core from the stabilizing influence of the walls in the horizontal direction, while providing random finite-amplitude disturbances to the interior. We note that the r.m.s. disturbance temperature and vertical velocity distributions shown in figure 12 are in good qualitative agreement with eigenfunctions obtained by Gill & Davey (1969) from a linear stability study of the buoyancy layer in the presence of a uniform stable vertical temperature gradient. This agreement suggests that the linearly unstable modes may retain the same qualitative character well beyond the range of validity of the linearized theory.

To better understand the mechanisms of energy transfer, we write the turbulent boundary-layer equations governing the mean flow

$$\frac{\partial U_i}{\partial x_i} = 0, \tag{3.25}$$

$$\frac{\partial}{\partial x_i}(U_i V) = \frac{Ra\,Pr}{2}\theta + \frac{\partial}{\partial x}\left(-\overline{u'v'} + Pr\frac{\partial V}{\partial x}\right), \tag{3.26}$$

$$\frac{\partial}{\partial x_i}(U_i \theta) = \frac{\partial}{\partial x}\left(-\overline{u'\theta'} + \frac{\partial \theta}{\partial x}\right), \tag{3.27}$$

and the turbulent kinetic energy ($k = \frac{1}{2}u'_i u'_i$) and squared temperature fluctuations ($q = \frac{1}{2}\theta'^2$)

$$\frac{\partial}{\partial x_i}(U_i \bar{k}) = -\frac{\partial}{\partial x}(\overline{u'p'} + \overline{u'k}) + Pr\frac{\partial^2 \bar{k}}{\partial x_j \partial x_j} + \frac{Ra\,Pr}{2}\overline{v'\theta'} - \overline{u'v'}\frac{\partial V}{\partial x} - Pr\overline{\frac{\partial v'_i}{\partial x_j}}\,\overline{\frac{\partial v'_i}{\partial x_j}}, \tag{3.28}$$

$$\frac{\partial}{\partial x_i}(U_i \bar{q}) = -\frac{\partial}{\partial x}\overline{u'q} + \frac{\partial^2 \bar{q}}{\partial x_j \partial x_j} - \overline{u'\theta'}\frac{\partial \theta}{\partial x} - \overline{v'\theta'}\frac{\partial \theta}{\partial y} - \overline{\frac{\partial \theta'}{\partial x_j}}\,\overline{\frac{\partial \theta'}{\partial x_j}}. \tag{3.29}$$

The left-hand sides and the first two terms on the right-hand sides of (3.28) and (3.29) are terms that become zero when integrated over the whole flow. They represent the transfer of energy from place to place by the mean motion and by the turbulence itself. The last terms on the right-hand sides are always negative and thus represent viscous and conductive dissipation of turbulence, respectively. The input of energy to compensate for the dissipation must be provided by the two terms remaining on the right-hand sides of (3.28) and (3.29).

In figure 15 we display the computed turbulent shear stress and heat fluxes normalized in an appropriate fashion. In forced convection, the Reynolds stress correlates very closely with the mean vertical velocity gradient as $-\overline{u'v'} > 0$ when $\partial V/\partial x > 0$ and $-\overline{u'v'} < 0$ when $\partial V/\partial x < 0$. Therefore, $-\overline{u'v'}$ usually becomes positive in the near-wall region of $\partial V/\partial x > 0$. However, the Reynolds stress near the wall in natural convection is almost zero in spite of $\partial V/\partial x > 0$. Upon integrating (3.26) from 0 to x and solving for $-\overline{u'v'}$, we see from figure 15 that the buoyancy contribution nearly cancels the contribution due to viscous diffusion. As the location of maximum vertical velocity is approached, the buoyancy contribution increases faster than the viscous diffusion term, leading to a decrease in $-\overline{u'v'}$. Consequently, the maximum velocity location x_{M} (where $\partial V/\partial x = 0$) does not coincide with the location of $\overline{u'v'} = 0$. The outer layer has the same characteristic as the forced-convection boundary layer since there $\partial V/\partial x < 0$ and $-\overline{u'v'} < 0$. From figure 14 and (3.28) we see that the double-peak behaviour of the turbulent kinetic energy is closely tied to the behaviour of the source term $\overline{v'\theta'}$. This term is dominant where $\partial V/\partial x \approx 0$ (i.e. near the location of maximum velocity and near the edge of the boundary layer). From figures 14 and 15 we see a direct correspondence between the maxima in $\overline{v'\theta'}$ and those in $\bar{k}$. In between the peaks in $\bar{k}$, $\partial V/\partial x$ is not zero, and so the more complicated behaviour results from the balance of both source terms with viscous dissipation.

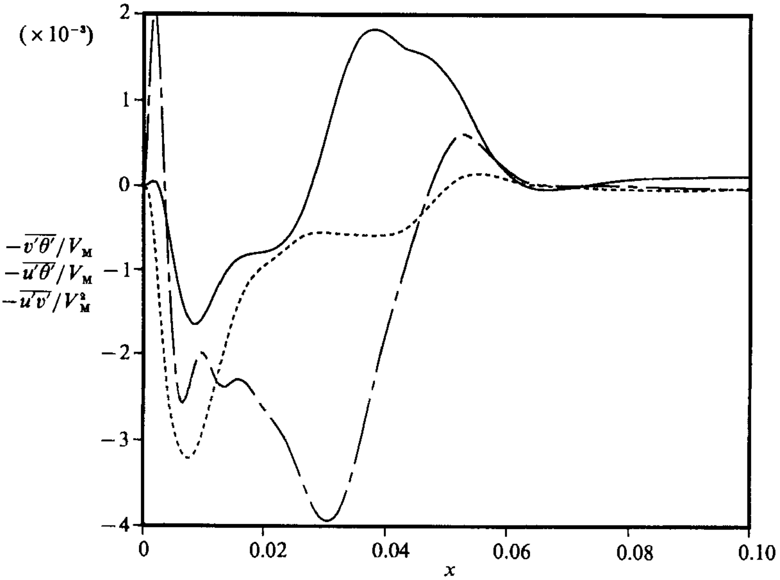

FIGURE 15. Distributions of Reynolds stress and turbulent heat fluxes at the mid-height of the cavity and in the vicinity of the hot wall: ———, $-\overline{u'v'}/V_M^2$; – – –, $-\overline{u'\theta'}/V_M$; ·········, $-\overline{v'\theta'}/V_M$.

Similarly, upon integrating (3.27) from 0 to x and solving for the turbulent heat flux $-\overline{u'\theta'}$, we see that near the wall the advection term is small and so $-\overline{u'\theta'}$ decreases largely in accordance with the thermal conduction term. From (3.29) we see that $-\overline{u'\theta'}\,\partial\theta/\partial x$ is a source of squared temperature fluctuations $\overline{q}$. Note that this source is much larger than the other source term $-\overline{v'\theta'}\,\partial\theta/\partial y$ since $\partial\theta/\partial x \gg \partial\theta/\partial y$ in this region. Therefore, from figures 12 and 15 we see that the maximum intensity of temperature fluctuations occurs near the location where $-\overline{u'\theta'}\,\partial\theta/\partial x$ is maximum. The value of $-\overline{u'\theta'}$ becomes a minimum with the increase of the advection term in the vicinity of the maximum vertical velocity location x_M (see figure 7), and then increases toward zero at the outer edge of the boundary layer, where advection and diffusion balance. The distribution of squared temperature fluctuations is a little complicated as the edge of the boundary layer is approached since $\partial\theta/\partial x$ becomes comparable with $\partial\theta/\partial y$ in this region, and so both source terms contribute in the balance with the diffusion term. The distribution of $-\overline{u'\theta'}$ is similar to that observed in forced convection.

For $x > 0.065$ turbulence production is small but not insignificant, since in that region the mean velocities are zero and the mean temperature is constant in the horizontal direction. The r.m.s. velocity fluctuations in the core of the cavity are small and relatively constant as hinted by figure 12. At the centre they are $(\overline{u'^2})^{\frac{1}{2}}/V_M \approx 0.024$, and $(\overline{v'^2})^{\frac{1}{2}}/V_M \approx 0.011$. The temperature fluctuations in the same region are also approximately constant but less than 1% ($(\overline{\theta'^2})^{\frac{1}{2}} \approx 0.002$), indicating that the thermal fluctuations are highly damped by the stable vertical stratification.

From integrals of the autocorrelation coefficients of T, u, and v, we have obtained respective estimates for the integral timescales (measured on a diffusion timescale) at several locations on the mid-height of the cavity. Consistent with expectations, the resulting estimates vary from approximately 2×10^{-6} in the vicinity of the active walls, to 4×10^{-5} in the centre of the cavity. Based on these estimates, we see that the sampling period (at statistical steady state) encompasses from approximately 140 eddy turnovers near the active walls to 7 turnovers near the centre.

3.5. *Probability density and energy spectra*

In figure 16 the calculated probability density distributions of temperature and velocity are shown at selected locations on the mid-height of the cavity. $P(g)$ is normalized such that $\int_{-\infty}^{+\infty} P(g)\,\mathrm{d}g = 1$. Greater intensity of fluctuations is indicated by the greater width of a distribution and correspondingly smaller values of P. This is clearly seen by identifying the locations of distributions with those in figures 12–14. Thus, as observed previously, fluctuations in the sublayer and mixing region are the strongest. From the distributions of temperature fluctuations we see that fluid in the outer portion of the boundary layer does not penetrate beyond the boundary of the buoyant sublayer. Note further that both in the core of the cavity and in the middle of the mixing region the probability distributions are symmetrical. As the wall is approached, the distributions become more and more asymmetric owing to intermittency of the flow, and finally develop a bimodal character arising from the oscillatory nature of the folding process. Except for presence of a bimodal distribution close to the walls, the results for $P(T)$ are in qualitative agreement with those of Elder (1965*b*) and Kirdyashkin *et al.* (1983). Note that the presence of a bimodal distribution depends not only on the location within the cavity, but also requires good resolution in the measurements.

To the author's knowledge, no experimental probability distribution is available for velocity. From figure 16 we see that $P(u)$ remains fairly symmetric about $u = 0$ and is broadest near the edge of the boundary layer where the horizontal fluctuations are largest (see figure 12). We also observe that the periodic oscillations due to the folding process are felt very close to the wall and result in the bimodal distribution of $P(v)$ there. $P(v)$ remains fairly broad and retains the multimodal character as the edge of the boundary layer is approached. However, note that near $x = 0.03$ the vertical velocity fluctuations are highly damped by the stable stratification, resulting in a peaked bimodal distribution with a zero mean near that location. From the distribution of $P(u)$ and $P(v)$ near the centre of the cavity we note that while the means of both velocity components are zero, the fluctuations are not. Furthermore, owing to the stable vertical stratification, the horizontal fluctuations are substantially larger than the vertical ones, as expected.

The spectral densities of temperature and velocity fluctuations are shown in figure 17 at the same selected points. From the figure we observe that even though the spectra are continuous, dominant peaks occur near frequencies of 11650 and 90300. These frequencies have been shown by PC to correspond to the characteristic frequencies of internal waves and boundary-layer instability, respectively. Owing to the presence of the stable stratification in the core of the cavity and the large vertical velocity next to the active walls, fluctuations in the velocity field are constrained. In the core of the cavity, the flow can only execute low-frequency fluctuations since it is removed from any source of turbulence in addition to feeling the full impact of the stratification. As we move towards the vertical walls, the longitudinal component of velocity can only perform low-frequency oscillations in the middle of the boundary layers since it has to overcome the stabilizing effects of stratification and viscous damping, while the horizontal component oscillates at higher frequencies in the mixing region since it only has to overcome damping effects due to the wall. Owing to wall damping, the energy at the lowest frequencies decreases as the wall is approached, explaining our previous observation that the maximum amplitude of

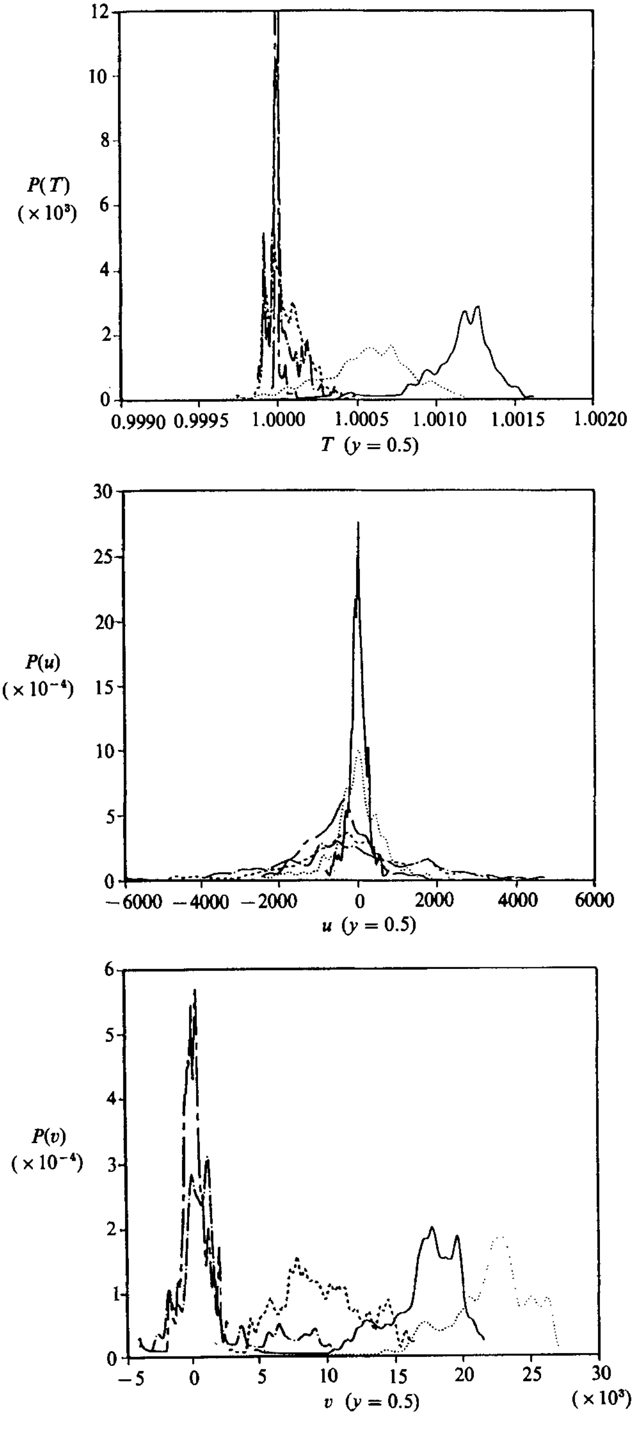

FIGURE 16. Temperature and velocity probability distributions at the mid-height of the cavity: ———, $x = 0.002$; ······, $x = 0.005$; ----, $x = 0.015$; —·—·, $x = 0.030$; ——— —, $x = 0.500$.

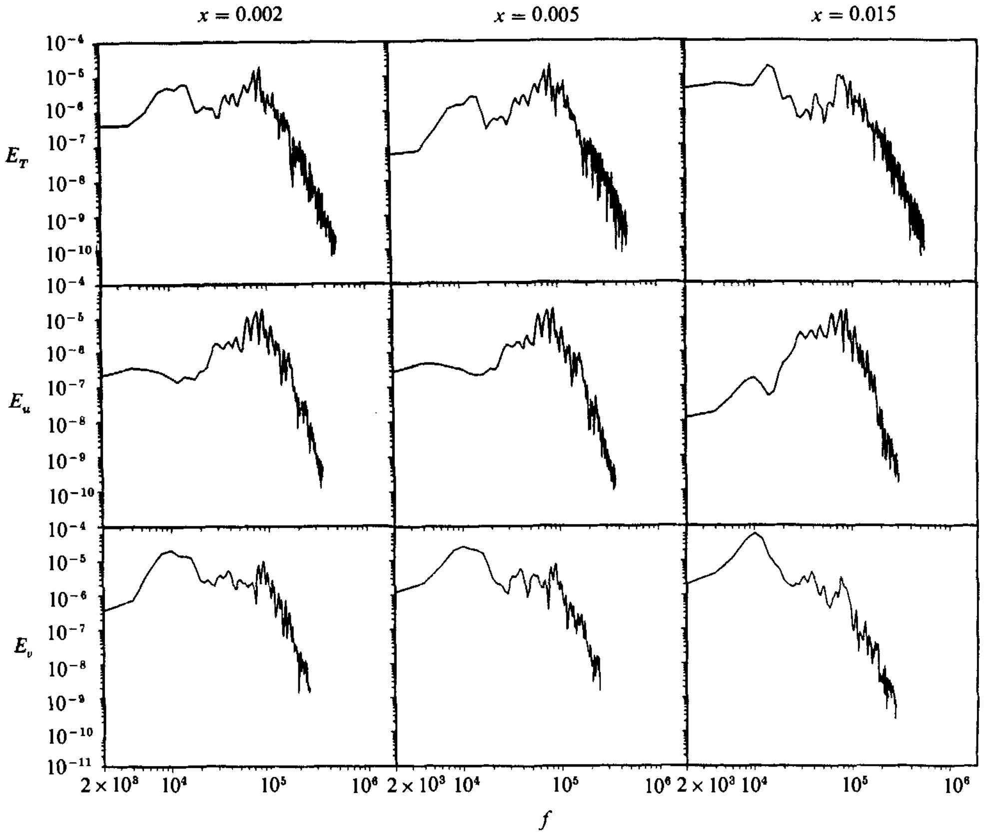

FIGURE 17. For caption see facing page.

fluctuations of the horizontal component of velocity occurs substantially further from the wall than that for the vertical component. The velocity fluctuations are clearly felt by the temperature field as evident from the figure.

Our results, which are for $Ra_y = 1.25 \times 10^9$, are consistent with the experimental data of Kirdyashkin & Semenov (1984). At $Ra_y = 10^9$ their results show a local minimum in the temperature energy spectrum between the low- and high-frequency peaks. At $Ra_y = 9 \times 10^{10}$ this minimum disappears resulting in an approximately constant energy region between these two characteristic frequencies. No spectral data for velocity are given in their work.

We note that the high-frequency turbulent energy, which is generated near the active walls at small scales, cascades towards low-frequency large scales in the core of the cavity. This process is in accord with the two-dimensional turbulence picture of Kraichnan (1967) and Lilly (1969) who show that in inviscid isothermal flow the cascade of energy is mainly toward low wavenumber in the inertial range, and becomes weak or non-existent at higher wavenumbers where only vorticity variance or enstrophy is cascaded in the usual sense in the inertial range.

4. Conclusions

Convection flow in a vertical layer for Rayleigh numbers in the turbulent regime passes through several stages. In the lower part of the cavity, next to the heated wall,

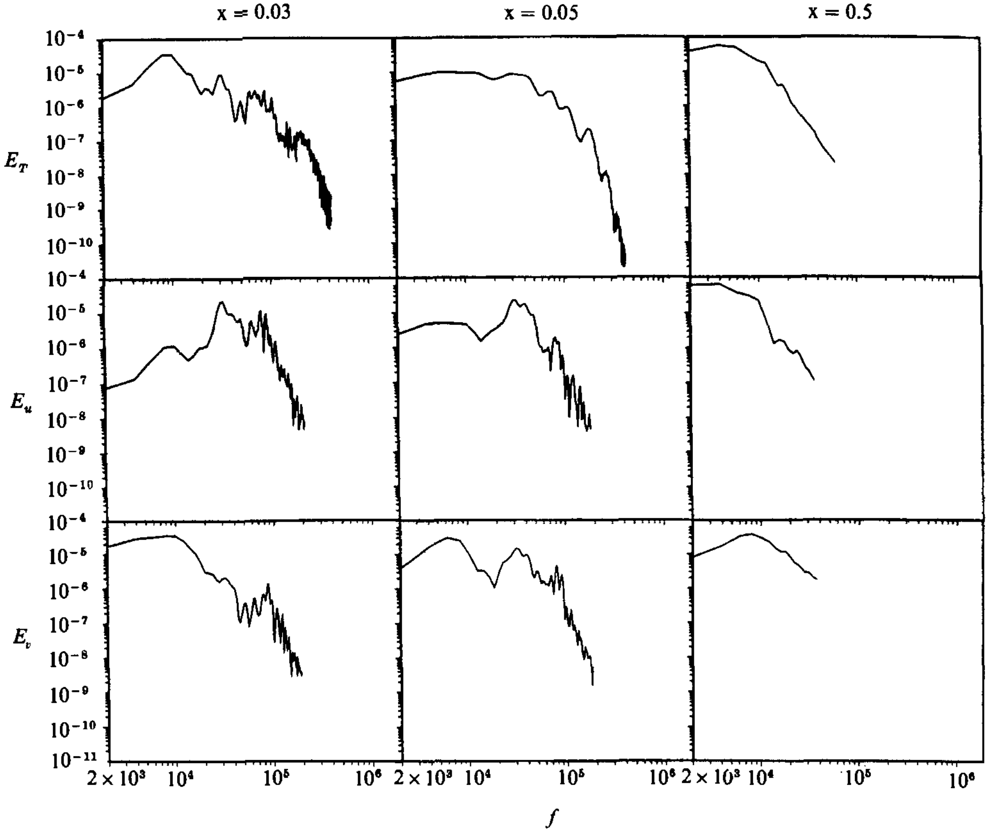

FIGURE 17. Temperature and velocity energy spectra at the mid-height of the cavity at x locations labelled on the figure.

the boundary-layer flow has a laminar character. This region is immediately followed by transition and finally by a turbulent boundary layer. The space between the vertical boundary layers is filled by a virtually immobile stably stratified fluid executing low-frequency, low-velocity oscillations. This central core is continually stirred by random buoyant elements of finite energy which are discharged into it.

It was shown that the thermal and momentum boundary layers can each be characterized by three regions. Directly against the wall there are the conductive and viscous sublayers, where the heat flux is constant but the shear stress is not. In these regions we see a monotonic rise in the intensity of fluctuations. These regions are followed by the momentum and thermal buoyant sublayers whose variation with distance from the wall depend on $+\frac{1}{3}$ and $-\frac{1}{3}$ powers, respectively. Thermal energy transferred by conduction accumulates in the thermal sublayer giving rise to fluctuations which constitute a considerable part of the heat transfer. Exterior to the mean vertical velocity maximum we have shown that the velocity distribution is self-similar. In this strong mixing region wave-like structures are superimposed on the mean motion. As elements of these structures accelerate out of the region a local reduction of the thermal energy is observed. The elements move sufficiently rapidly out of this highly intermittent region for molecular processes to be negligible. The external part of the thermal boundary layer is characterized by a small value of excess mean temperature.

The stable stratification of the fluid outside the boundary layers significantly affects the nature of the flow, but has no effect on the heat transfer and momentum in the conductive and viscous sublayers.

An attempt was made to compare predictions with available experimental evidence. It was seen that many of the computational results could be substantiated either directly or upon replotting data available in the literature. In particular, the heat transfer law, the vertical stratification in the core, the viscous and conducting sublayers, the existence of momentum and thermal buoyant sublayers, and the self-similar distribution of the outer boundary-layer region are in good quantitative agreement with available data. Many of the features observed in the flow such as the sinusoidal mode of instability, the internal jumps in the departing corners, and the hook-like structures have been observed experimentally. However, the validity of many other results can only be verified when more experimental data becomes available.

Finally, we must note that some of the results obtained in the present work may be applicable to other turbulence problems where buoyancy and stable stratification play essential roles. For example, it was first noted by Elder (1965*b*), upon close inspection of the ideas of thermal turbulence proposed by Priestley (1959), that the angles between the directions of gravity and mean heat flux are not invoked. Priestley argued that for fully turbulent free convective flow from a flat surface there must exist a region of the flow following a constant heat flux layer which is characterized only by the heat flux, the buoyancy parameter, and the distance from the surface. It follows immediately on dimensional grounds that the profile of temperature in this region must depend on the inverse cube root of the distance from the wall. Although Priestley's arguments were made in connection with atmospheric flows, Elder realized the applicability of the results to a differentially heated cavity.

A portion of these results were presented by the author at the American Physical Society/Fluid Dynamics Division Annual Meeting held in Tucson, Arizona, 24–27 November 1985. I would like to thank Dr D. R. Chenoweth for invaluable discussions on some aspects of this work. This work was performed under the auspices of the US Department of Energy by Sandia National Laboratories, Livermore, California, under Contract No. DE-AC04-76DP00789.

REFERENCES

Batchelor, G. K. 1954 Heat transfer by free convection across a closed cavity between vertical boundaries at different temperatures. *Q. Appl. Maths* **12**, 209–233.

Cheesewright, R. 1968 Turbulent natural convection from a vertical plane surface. *Trans. ASME* C: *J. Heat Transfer* **90**, 1–8.

Cheesewright, R. & Ierokiopitis, E. 1982 Velocity measurements in a turbulent natural convection boundary layer. In *Heat Transfer 1982* (ed. U. Grigull, E. Hahne, K. Stephan & J. Straub), vol. 2, pp. 305–309.

Chenoweth, D. R. & Paolucci, S. 1981 On optimizing nonuniform finite-difference grids for boundary regions in transient transport problems. *Sandia National Laboratories Rep.* SAND81-8204.

Chenoweth, D. R. & Paolucci, S. 1986 Natural convection in an enclosed vertical air layer with large horizontal temperature differences. *J. Fluid Mech.* **169**, 173–210 (referred to as CP).

Cormack, D. E., Leal, L. G. & Imberger, J. 1974 Natural convection in a shallow cavity with differentially heated end walls. Part 1. Asymptotic theory. *J. Fluid Mech.* **65**, 209–229.

Corrsin, S. 1961 Turbulent flow. *Am. Sci.* **49**, 300–325.

COWAN, G. H., LOVEGROVE, P. C. & QUARINI, G. L. 1982 Turbulent natural convection heat transfer in vertical single water-filled cavities. In *Heat Transfer 1982* (ed. U. Grigull, E. Hahne, K. Stephan & J. Straub), vol. 2, pp. 195–203.

ECKERT, E. R. G. & CARLSON, W. O. 1961 Natural convection in an air layer enclosed between two vertical plates with different temperatures. *Intl J. Heat Mass Transfer* **2**, 106–120.

ELDER, J. W. 1965*a* Laminar free convection in a vertical slot. *J. Fluid Mech.* **23**, 77–98.

ELDER, J. W. 1965*b* Turbulent free convection in a vertical slot. *J. Fluid Mech.* **23**, 99–111.

FUJII, T., TAKEUCHI, M., FUJII, M., SUZAKI, K. & UEHARA, H. 1970 Experiments on natural-convection heat transfer from the outer surface of a vertical cylinder to liquids. *Intl J. Heat Mass Transfer* **13**, 753–787.

GEORGE, W. K. & CAPP, S. P. 1979 A theory for natural convection turbulent boundary layers next to heated vertical surfaces. *Intl J. Heat Mass Transfer* **22**, 813–826.

GIEL, P. W. & SCHMIDT, F. W. 1986 An experimental study of high Rayleigh number natural convection in an enclosure. In *Heat Transfer 1986* (ed. C. L. Tien, V. P. Carey & J. K. Ferrell), vol. 4, pp. 1459–1464.

GILL, A. E & DAVEY, A. 1969 Instabilities of a buoyancy-driven system. *J. Fluid Mech.* **35**, 775–798.

GOLDSTEIN, S. 1938 *Modern developments in fluid dynamics*, Vol. II. Oxford University Press.

GRÖTZBACH, G. 1982 Direct numerical simulation of laminar and turbulent Bénard convection. *J. Fluid Mech.* **119**, 27–53.

GRÖTZBACH, G. 1983 Spatial resolution requirements for direct numerical simulation of the Rayleigh–Bénard convection. *J. Comput. Phys.* **49**, 241–264.

IVEY, G. N. 1984 Experiments on transient natural convection in a cavity. *J. Fluid Mech.* **144**, 389–401.

JAKOB, M. 1949 *Heat Transfer*. Wiley.

KIRDYASHKIN, A. G. & SEMENOV, V. I. 1984 Spectra of temperature fluctuations in a vertical layer with thermogravitational convection. *High Temp.* **21**, 558–565.

KIRDYASHKIN, A. G., SEMENOV, V. I., BERDNIKOV, V. S. & GAPONOV, V. A. 1983 Structure of the temperature field in a vertical layer with thermal gravitational convection. *High Temp.* **20**, 750–757.

KRAICHNAN, R. H. 1967 Inertial ranges in two-dimensional turbulence. *Phys. Fluids* **10**, 1417–1423.

KUTATELADZE, S. S., IVAKIN, V. P., KIRDYASHKIN, A. G. & KEKALOV, A. N. 1977 Turbulent natural convection in a vertical layer. *High Temp.* **15**, 458–464.

KUTATELADZE, S. S., IVAKIN, V. P., KIRDYASHKIN, A. G. & KEKALOV, A. N. 1978 Thermal free convection in a liquid in a vertical slot under turbulent flow conditions. *Heat Transfer Soviet Res.* **10**, 118–125.

KUTATELADZE, S. S., KIRDYASHKIN, A. G. & IVAKIN, V. P. 1972*a* Turbulent natural convection at an isothermal vertical plate. *High Temp.* **10**, 76–79.

KUTATELADZE, S. S., KIRDYASHKIN, A. G. & IVAKIN, V. P. 1972*b* Turbulent natural convection on a vertical plate and in a vertical layer. *Intl J. Heat Mass Transfer* **15**, 193–202.

KUTATELADZE, S. S., KIRDYASHKIN, A. G. & IVAKIN, V. P. 1975 Turbulent natural convection at a vertical isothermal plate. *Sov. Phys. Dokl.* **19**, 480–482.

LIGHTHILL, J. 1978 *Waves in Fluids*. Cambridge University Press.

LILLY, D. K. 1965 On the computational stability of numerical solutions of time-dependent non-linear geophysical fluid dynamics problems. *Mon. Weather Rev.* **93**, 11–26.

LILLY, D. K. 1969 Numerical simulation of two-dimensional turbulence. *Phys. Fluids Suppl. II* **12**, 240–249.

LIPPS, F. B. 1976 Numerical simulation of three-dimensional Bénard convection in air. *J. Fluid Mech.* **75**, 113–148.

LOCHET, R., LEMONNIER, D. & DOAN-KIM-SON 1983 Correlations en convection naturelle turbulente. Influence de la pression et de la nature du gaz. *Intl J. Heat Mass Transfer* **26**, 1221–1227.

LOVE, M. D. 1979 An introduction to the large eddy simulation technique. *J. Inst. Nucl. Engrs* **20**, 35–42.

MacGregor, R. K. & Emery, A. F. 1969 Free convection through vertical layers – Moderate and high Prandtl number fluids. *Trans. ASME* C: *J. Heat Transfer* **91**, 391–401.

Mordchelles-Regnier, G. & Kaplan, C. 1963 Visualization of natural convection on a plane wall and in a vertical gap by differential interferometry: transitional and turbulent regimes. In *1963 Heat Transfer and Fluid Mech. Inst.*, pp. 94–111. Stanford University Press.

Paolucci, S. 1982 On the filtering of sound from the Navier–Stokes equations. *Sandia National Laboratories Rep.* SAND82-8257.

Paolucci, S. & Chenoweth, D. R. 1989 Transition to chaos in a differentially heated vertical cavity. *J. Fluid Mech.* **201**, 379–410 (referred to as PC).

Pirovano, A., Viannay, S. & Jannot, M. 1970 Convection naturelle en regime turbulent le long d'une plaque plane verticale. In *Heat Transfer 1970* (ed. V. Grigull & E. Hahne), vol. 4, pp. 1–12.

Plumb, O. A. 1976 An experimental and numerical examination of buoyancy driven wall boundary layers. Ph.D. Thesis, State University of New York at Buffalo.

Priestley, C. B. H. 1959 *Turbulent Transfer in the Lower Atmosphere.* Chicago University Press.

Schumann, U., Grötzbach, G. & Kleiser, L. 1980 Direct numerical simulation of turbulence. In *Prediction Methods for Turbulent Flows* (ed. W. Kollmann), pp. 123–258. Hemisphere.

Siebers, D. L., Moffatt, R. F. & Schwind, R. G. 1985 Experimental, variable properties natural convection from a large, vertical, flat surface. *Trans. ASME* C: *J. Heat Transfer* **107**, 124–132.

Smith, R. R. 1972 Characteristics of turbulence in free convection flow past a vertical plate. Ph.D. Thesis, University of London.

Tzuoo, K. L., Chen, T. S. & Armaly, B. F. 1985 Wave instability of natural convection flow on inclined surfaces. *Trans. ASME* C: *J. Heat Transfer* **107**, 107–111.

Vahl Davis, G. de & Jones, I. P. 1983 Natural convection in a square cavity: a comparison exercise. *Intl J. Numer. Meth. Fluids* **3**, 227–248.